



HAL
open science

Joint inversion of ground gravity data and satellite gravity gradients between Nepal and Bhutan: New insights on structural and seismic segmentation of the Himalayan arc

Rodolphe Cattin, Théo Berthet, György Hetényi, Anita Saraswati, Isabelle Panet, Stéphane Mazzotti, Cécilia Cadio, Matthieu Ferry

► To cite this version:

Rodolphe Cattin, Théo Berthet, György Hetényi, Anita Saraswati, Isabelle Panet, et al.. Joint inversion of ground gravity data and satellite gravity gradients between Nepal and Bhutan: New insights on structural and seismic segmentation of the Himalayan arc. *Physics and Chemistry of the Earth. Parts A/B/C*, 2021, 123, pp.103002. 10.1016/j.pce.2021.103002 . hal-03400304

HAL Id: hal-03400304

<https://hal.science/hal-03400304>

Submitted on 22 Aug 2023

HAL is a multi-disciplinary open access archive for the deposit and dissemination of scientific research documents, whether they are published or not. The documents may come from teaching and research institutions in France or abroad, or from public or private research centers.

L'archive ouverte pluridisciplinaire **HAL**, est destinée au dépôt et à la diffusion de documents scientifiques de niveau recherche, publiés ou non, émanant des établissements d'enseignement et de recherche français ou étrangers, des laboratoires publics ou privés.



Distributed under a Creative Commons Attribution - NonCommercial 4.0 International License

1 **Joint inversion of ground gravity data and satellite gravity gradients**
2 **between Nepal and Bhutan: New insights on structural and seismic**
3 **segmentation of the Himalayan arc**

4 Cattin Rodolphe¹, Berthet Théo², Hetényi György³, Saraswati Anita^{1,4}, Panet Isabelle^{5,6},
5 Mazzotti Stéphane¹, Cadio Cécilia¹, Ferry Matthieu¹

6 ¹ Géosciences Montpellier, Université de Montpellier, CNRS, Montpellier, France

7 ² Department of Earth Sciences, Uppsala University, Villavägen 16, 75236 Uppsala, Sweden

8 ³ Institute of Earth Sciences, University of Lausanne, Géopolis, Quartier UNIL-Mouline, 1015
9 Lausanne, Switzerland

10 ⁴ Faculty of Sciences, Technology and Medicine, Université du Luxembourg, L-4364 Esch-sur-
11 Alzette, Luxembourg

12 ⁵ Université de Paris, Institut de physique du globe de Paris, CNRS, IGN, F-75005 Paris, France

13 ⁶ ENSG-Géomatique, IGN, F-77455 Marne-la-Vallée, France

14

15

16 Corresponding author: Rodolphe Cattin (rodolphe.cattin@umontpellier.fr)

17 **Abstract**

18 Along-strike variation in the geometry of lithospheric structures is a key control parameter for the
19 occurrence and propagation of major interplate earthquakes in subduction and collision zones.
20 The lateral segmentation of the Himalayan arc is now well-established from various
21 observations, including topography, gravity anomalies, exhumation rates, and present-day
22 seismic activity. Good knowledge of the main geometric features of these segments and their
23 boundaries is thus the next step to improve seismic hazard assessment in this area. Following

24 recent studies, we focus our approach on the transition zone between Nepal and Bhutan where
25 both $M > 8$ earthquakes and changes in the geometry of the Indian plate have been documented.
26 Ground gravity data sets are combined with satellite gravity gradients provided by the GOCE
27 mission (Gravity Field and Steady-State Ocean Circulation Explorer) in a joint inversion to
28 assess the location and the geometry of this transition. We obtain a ca. 10 km wide transition
29 zone located at the western border of Bhutan that is aligned with the Madhupur fault in the
30 foreland and coincides with the Dhubri–Chungthang fault zone and the Yadong-Gulu rift in
31 Himalaya and southern Tibet, respectively. This sharp segment boundary at depth can act as a
32 barrier to earthquake rupture propagation. It can possibly restrict the size of large earthquakes
33 and thus reduce the occurrence probability of $M > 9$ earthquakes along the Main Himalayan
34 Thrust.

35

36 **1. Introduction**

37 It is well-established that along-strike variations of megathrusts in both subduction and collision
38 zones are key parameters which control the location and size of major earthquakes.

39 Over the last two decades, several great earthquakes ($M > 8$) have been documented in
40 Himalayas along the Main Frontal Thrust (MFT) from paleoseismic studies (e.g. Nakata et al.,
41 1998; Lavé et al., 2005; Kumar et al., 2010; Mugnier et al., 2013; Sapkota et al., 2013; Bollinger
42 et al., 2014; Rajendran et al., 2015; Le Roux–Mallouf et al., 2016, 2020; Wesnousky et al.,
43 2017a, b, 2018, 2019). Lavé et al. (2005) suggested that at least one great earthquake with an
44 estimated vertical slip component of 7–7.5 m (and an inferred total coseismic displacement on
45 the order of 17 m) ruptured a large segment of the Himalayan arc around 1100 in central Nepal.
46 Further east, Sapkota et al. (2013) documented at least one great earthquake before 1300 with
47 an estimated vertical slip component between 3 m and 8 m (and an inferred total coseismic

48 displacement between 5 m and 17 m). Additionally, Kumar et al. (2010) described co-seismic
49 displacements larger than 12 m both East and West of Bhutan, with possibly contemporaneous
50 age constraints. Le Roux-Mallouf et al. (2016) documented also a great earthquake in Bhutan
51 which occurred between 1140 and 1520 with ~8 m of vertical offset. More recently, Wesnousky
52 et al. (2017b, 2018, 2019) completed this catalog by studying three sites in central eastern
53 Nepal showing vertical coseismic slip of about 7 m compatible with an earthquake in ca. 1100
54 (figure 1).

55 During the same period, many studies in thermochronology, geomorphology and geophysics
56 have revealed the segmented nature of the Himalayan arc in terms of along-strike variations of
57 tectonic structures (e.g. Duncan et al., 2003; Robert et al., 2011; Hetényi et al., 2016; Dal Zilio
58 et al., 2020). However, the main geometric features of the boundaries of these segments remain
59 poorly constrained. For instance, Duncan et al. (2003) showed a clear difference in the
60 topographic profiles across central Nepal and Bhutan. Based on low temperature
61 thermochronology data and associated exhumation rates, Robert et al. (2011) suggested also
62 along-strike variations in the geometry of crustal-scale faults between central Nepal and Bhutan.
63 These two studies are focused on individual sections across the belt and do not provide
64 information about the transition itself, neither on its location nor on its width.

65 This lack of information represents a major limitation for seismic hazard assessment along the
66 Himalayan arc and prevents any interpretation of past major earthquake sequences in terms of
67 geometric segmentation. In this study, we focus on the area between central Nepal and Bhutan,
68 where major lateral variations as well as seismic segmentation have been already documented.
69 First, we fix the lithospheric structure's geometry of each segment from available 2D images of
70 the underthrusting Indian plate across central Nepal and western Bhutan. Next, after synthetic
71 tests, we assess the main geometric features of this boundary from a joint approach using both
72 ground and satellite gravity data sets. Finally, we discuss the structural control of this segment

73 boundary on present-day deformation and its relationship with the propagation of major
74 historical earthquakes between Nepal and Bhutan.

75 **2. Method and data**

76 **2.1. Evidences of along-strike discontinuity**

77 Although the tectonic units are remarkably continuous along the 2400 km long shape of the
78 Himalayas, a growing number of studies suggest the existence of lateral variations, especially
79 between central Nepal and Bhutan. Duncan et al. (2003) were the first to highlight along-strike
80 variations by showing differences in the patterns of topographic profiles between Nepal and
81 Bhutan. Since this pioneering study, detailed geologic mapping and thermochronological data
82 have underlined along-strike changes in the stratigraphy and structure between these two
83 regions (e.g. McQuarrie et al., 2008; Robert et al., 2011). Based on geophysical information,
84 Gahalaut and Arora (2012) propose a control of these inherited structures on seismic
85 segmentation marked by a low present-day seismicity rate in Bhutan compared to the Nepal
86 segment. The analysis of arc-parallel gravity anomalies highlights also lateral variations in the
87 geometry of the foreland basin as well as in the deep structure of the orogen between Nepal
88 and Bhutan (Hetényi et al., 2016). More recently, Dal Zilio et al. (2020) show a clear zonation of
89 interseismic coupling inferred from geodetic data, with a high coupling of ca. 0.8 in Nepal
90 compared to ca. 0.5 in western and central Bhutan.

91 **2.2. Approach strategy**

92 No studies to date, however, have focused on the main geometric features of this transition
93 zone between central and eastern Himalaya. First, to better assess its precise location as well
94 as its lateral extension, we consider two master profiles across the range:

95 - For the Nepal segment, many structural geology field campaigns as well as
96 seismological experiments were performed to image the main structures (e.g. Le Fort,
97 1975; Schulte-Pelkum et al., 2005; Nábělek et al., 2009). The geometry of major faults,
98 the depth of both the Moho and the foreland sedimentary basin as well as the physical
99 properties of crust and mantle are now relatively well-known. In the following, we use the
100 results obtained by Berthet et al. (2013) from ground gravity measurements in Nepal
101 between longitude 83° and 86.5°. This profile (BP hereinafter) is a cross-section through
102 the range at the longitude of Kathmandu (see location figure 1). This profile is consistent
103 with previous geological and seismological results and provides information about
104 density layering (figure 2).

105 - For the Bhutan segment, fewer studies have been conducted. Nevertheless, recent
106 thermochronological data (e.g. McQuarrie et al., 2008, 2015; Coutand et al., 2014),
107 geomorphological observations (Le Roux-Mallouf et al., 2015) and geophysical works
108 (Hammer et al., 2013; Singer et al., 2017; Diehl et al., 2017) allow constraining the
109 geometry of deep structures in west-central Bhutan. In the following, we use the profile
110 obtained by Hammer et al. (2013) from ground gravity measurements (figure 2). This
111 profile (HP hereinafter) is a cross-section through the range at the longitude of the city of
112 Wangdue Phodrang (see location figure 1).

113 These two model profiles (HP and BP) have many similarities: a comparable north-south
114 extension, the bending of the Indian plate under Tibet associated with an eclogitization of the
115 Indian lower crust, and an identical Moho depth under central Tibet. They also have their own
116 characteristics with a smaller and shallower foreland basin, a shorter flexural wavelength, and a
117 eclogitized zone reaching further south in Bhutan compared to Nepal (figure 2), although this
118 feature is included in a simplified way in both models compared to a petrologically constrained
119 model presented in Hetényi et al. (2007) .

120 Second, to extend laterally these two profiles, we use additional cross-sections defined with a
121 weighting coefficient α between Berthet's and Hammer's profiles:

122

$$(long, lat)_{profile} = \frac{1}{100} [(100 - \alpha) \times (long, lat)_{BP} + \alpha \times (long, lat)_{HP}], \quad (1)$$

123

124 where $long$ is the longitude and lat the latitude of points of profiles. $\alpha = 0$ and $\alpha = 100$ are
125 associated with BP and HP, respectively (figure 3a). Next, we define α_{west} and α_{east} for the
126 relative position of the eastern and the western boundaries of the transition zone. Assuming that
127 the transition zone is located between BP and HP, these two coefficients range between 0 and
128 100 and by definition $\alpha_{west} < \alpha_{east}$. In a $(\alpha_{west}, \alpha_{east})$ diagram, the lines parallel to the first
129 bisector ($\alpha_{east} - \alpha_{west} = constant$) are associated with transition zones with the same width,
130 whereas the lines perpendicular to the first bisector are related to transition zones with the same
131 mid-profile ($[\alpha_{east} + \alpha_{west}]/2 = constant$). Although a linear relationship exists between the α
132 coefficients and the geometry properties of the transition zone (figure 4), in the following we will
133 use these coefficients because they are more suitable for defining a 3D geometry. We create a
134 mesh model assuming a lateral uniformity between $\alpha = 0$ and α_{west} as well as between α_{east}
135 and $\alpha = 100$. We consider a linear interpolation between α_{west} and α_{east} using 10 profiles to
136 create a locally refined mesh for the transition zone (figure 3b). Two additional far-field profiles
137 are used to reduce boundary effects.

138 Finally, the gravity effect due to the meshed lithospheric bodies is calculated using the GEEC
139 software, which enables to compute both the gravity field and the full-tensor gravity gradient due
140 to irregularly shaped body mass (Saraswati et al., 2019). The results obtained by varying α_{west}
141 and α_{east} are then compared with gravity data sets, which include ground Bouguer anomaly
142 measurements and satellite gravity gradients (see flow chart on figure 5).

143 **2.3. Ground gravity data set**

144 The terrestrial gravity data set used in this study comes from the compilation published by
145 Hetényi et al. (2016). It was based on already available data from the International Gravimetric
146 Bureau (BGI, <http://bgi.omp.obs-mip.fr/>) and published studies (Das et al., 1979, Sun, 1989;
147 Banerjee, 1998, Martelet et al., 2001, Tiwari et al., 2006). This data set has been completed
148 with field measurements performed in Nepal (Berthet et al., 2013) and Bhutan (Hammer et al.,
149 2013) for obtaining a better coverage on either side of the Himalayas as well as more than 10
150 profiles across the mountain belt (figure 1). All the data sets have been fully reprocessed in the
151 same manner using the GravProcess software (Cattin et al., 2015), resulting in a coherent data
152 set of 2,749 Bouguer anomalies g_z (figure 6). Together with the errors in the vertical position
153 and the low resolution of the SRTM digital elevation model in high relief areas, the discrepancy
154 between existing data sets lead to an average accuracy of a few mGal (<10 mGal) for this
155 compilation of ground gravity data.

156 **2.3. GOCE gravity gradients**

157 The satellite data used in this study are the GOCE (Gravity Field and Steady-State Ocean
158 Circulation Explorer) gravity gradients of level-2 product EGG_TRF_2 ([https://goce-
159 ds.eo.esa.int/oads/access/](https://goce-ds.eo.esa.int/oads/access/)). This type of data sets has been externally calibrated and corrected
160 to temporal gravity variations by the GOCE High Processing Facility (HPF) (Gruber et al., 2011).
161 The gravity gradients are provided in the Local North Oriented Frame (LNOF, see Fuchs &
162 Bouman, 2011). To maximize the signal-to-noise ratio, we consider the period between August
163 2012 and September 2013, for which the satellite operated in low orbit at an altitude as low as
164 224 km.
165 To assess the signal due to variations of structures at depth, we perform data reductions
166 (topographic effect) using the GEEC software with WGS84 as the reference ellipsoid (Saraswati

167 et al., 2019). Following this previous study, we consider a digital elevation for the entire Earth
168 with a resolution of 15 km, which we found as a good compromise between the computation
169 time and the result accuracy. These reductions are performed on data along the GOCE orbit to
170 avoid noise amplification due to the downward continuation to the Earth's surface.

171 The final satellite data set consists of 17,533 measurements of the nine components of gravity
172 gradient tensor $T_{ij} = \partial g_i / \partial x_j$. This tensor is symmetric, its trace is zero and we will focus on the
173 longitudinal variations along the Himalayan arc. Hence, in the following, we will only consider
174 four components that are T_{NW} , T_{WW} , T_{WZ} , and T_{ZZ} (figure 7), where N , W and Z are associated
175 with the North-West-Up local frame. Taking into account the uncertainties in the measurements
176 and the errors associated with both the ellipsoid model and the digital elevation model, an
177 average accuracy of 0.1 E is assumed hereinafter for the derived gravity gradient anomalies
178 (which are Bouguer anomalies).

179 **3. Synthetic tests**

180 In this section, we perform tests on synthetic models to assess how our approach allows finding
181 the geometry of a lateral crustal ramp located between the profiles of Berthet et al. (2013) and
182 Hammer et al. (2013). Using the gravity data sets described above, a systematic exploration of
183 the coefficients α_{west} and α_{east} are carried out to test the sensitivity of our inversion results to
184 the transition zone geometry parameters (location and width) as well as to the data
185 uncertainties.

186 **3.1. Synthetic inversion reference test**

187 First, we consider a lateral ramp located halfway between Berthet's and Hammer's profiles with
188 a width of ca. 250 km. This model corresponds to assuming $\alpha_{west} = 25$ and $\alpha_{east} = 75$ as initial
189 coefficients. Using the density distribution at depth of BP and HP, the gravity anomalies and the

190 gravity gradients are computed at the location of gravity measurements. A normal distributed
 191 random noise is added to these synthetic data sets with a mean of zero and a standard
 192 deviation of 10 mGal and 0.1 E for the Bouguer anomaly and gravity gradients, respectively.
 193 The inversion is performed with a systematic exploration of the coefficients α_{west} and α_{east} in a
 194 range between 0 and 100 with a step of 1. Knowing that $\alpha_{west} < \alpha_{east}$, for $\alpha_{west} = 0$ we test 100
 195 different $\alpha_{east} \in [1; 100]$ values, for $\alpha_{west} = 1$ only 99 values, and so on up to $\alpha_{west} = 99$ for
 196 which $\alpha_{east} = 100$. Hence we generate a collection of 5,050 models ($\sum_{k=1}^{100} k = \frac{100 \times 101}{2}$ models)
 197 and calculate for each of them their likelihood, which is defined as
 198

$$L(m) = \exp\left(-\frac{1}{n} \sum_{i=1}^n \left[\frac{calc_i - obs_i}{\sigma_i}\right]^2\right), \quad (2)$$

199
 200 where n is the number of data, $calc_i$ is the calculated gravity field (either Bouguer anomaly or
 201 gravity gradient component), obs_i is the observed gravity field (either Bouguer anomaly or
 202 gravity gradient component) and σ_i is the uncertainty, which is fixed to 10 mGal and 0.1 E for
 203 the Bouguer anomaly and gravity gradients, respectively.

204 As shown in figure 8, the obtained likelihood distribution is consistent with the initial coefficients
 205 $\alpha_{west} = 25$ and $\alpha_{east} = 75$. Our result underlines however the specific nature of each type of
 206 data, each providing different constraints on these two coefficients. Not surprisingly, the
 207 inversion of T_{NW} measurements gives a mostly constant likelihood because (1) g_N and g_W are
 208 low compared to g_Z and (2) the longitudinal variation in g_N or the latitudinal variation in g_W are
 209 not significantly affected by a lateral crustal ramp. Although the inversion of either T_{WW} or g_Z
 210 underestimates α_{west} and overestimates α_{east} , they provide good information on the location of
 211 the mid-profile of the transition zone. In contrast, T_{WZ} and T_{ZZ} are more suitable for finding

212 α_{east} and α_{west} , respectively. Irrespective of which data is used, the width of the transition zone
213 remains poorly constrained.

214 These results underline the strong nonuniqueness of the gravity inversion. This major limitation
215 can be reduced by a joint inversion, for which the best combinations of α_{west} and α_{east} are
216 obtained using simultaneously all the components of the gravity gradient tensor T_{ij} and the
217 Bouguer anomaly. To give the same weight for all data sets, the likelihood distribution is
218 normalized with the likelihood of the best-fitting model obtained for each data set. So the
219 normalized likelihood \underline{L} ranges between 0 and 1 and the likelihood associated with combined
220 data sets is simply the product of the likelihood obtained from each data set:

$$\begin{aligned} \underline{L(m)}_{T_{ij}} &= \underline{L(m)}_{T_{NW}} \times \underline{L(m)}_{T_{WW}} \times \underline{L(m)}_{T_{Wz}} \times \underline{L(m)}_{T_{ZZ}} \\ \text{and } \underline{L(m)}_{g_z \text{ and } T_{ij}} &= \underline{L(m)}_{g_z} \times \underline{L(m)}_{T_{ij}} \end{aligned} \quad (3)$$

222
223 In figure 8, the maximum of normalized likelihood ($\underline{L} > 0.9$) is found for $\alpha_{west} = 27 \pm 2$ and
224 $\alpha_{east} = 75 \pm 7$. These values are in good agreement with the initial coefficients. This first test
225 demonstrates the consistency of ground gravity data and satellite gravity gradients and the need
226 to invert them together. Furthermore, due to data distribution, this reference test suggests that
227 the western boundary is better constrained than the eastern one (Figure 8).

228 3.2. Effect of the lateral extension of the transition zone

229 In the reference synthetic test we considered a ca. 250 km wide transition zone. Here, we test
230 the influence of this zone's lateral extent in a range between ca. 2.5 km and ca. 490 km, all
231 other parameters remaining unchanged. Following the approach described in the previous
232 section, we generate synthetic data sets with a constant $\alpha_{mid-profile} = [\alpha_{west} + \alpha_{east}]/2 = 50$

233 and $\alpha_{east} - \alpha_{west} \in [0.5; 100]$. We then perform a similar inversion of both gravity and gravity
234 gradient data sets as above with a systematic exploration of the coefficients α_{west} and α_{east} .
235 Whichever the width considered, the maximum likelihood is obtained for α_{west} and α_{east} close to
236 the initial coefficients (Figure 9). The average standard deviation of the obtained $\alpha_{east} - \alpha_{west}$ is
237 6 (ca. 30 km). Our results suggest no obvious relationship between this standard deviation and
238 the lateral extent of the transition zone. Both for a very narrow (< 5 km) and a very wide (> 450
239 km) zone a low uncertainty (< 10 km) is obtained, while for an average width (ca. 200 km) the
240 standard deviation of this parameter can be significant and reach values up to ca. 75 km (Figure
241 9). This uncertainty is probably rather related to the heterogeneous distribution of ground gravity
242 data, which shows a gap in far east Nepal (Figure 6).

243 **3.3. Influence of the transition zone location**

244 We also study the influence of the location of the transition zone. As for the reference model, we
245 assume a ca. 250 km wide transition zone by testing models with mid-profiles located at
246 different positions between central-eastern Nepal and westernmost Bhutan ($[\alpha_{east} + \alpha_{west}]/2 \in$
247 $[25; 75]$).

248 The maximum likelihood for α_{west} and α_{east} coincides well with the initial coefficients (Figure
249 10). The standard deviation of the obtained location $[\alpha_{east} + \alpha_{west}]/2$ is 2 on average (ca. 10
250 km distance along the MFT) and can reach up to 4 (ca. 20 km distance along the MFT). These
251 two values are low compared to those obtained for the width, suggesting that the inversion of
252 gravity data gives better constraints on the mid-profile location than on the lateral extent of the
253 transition zone.

254 3.4. Sensitivity to the data uncertainties

255 In all previous synthetic tests, the inversions were performed with data uncertainties $\sigma_g = 10$
256 mGal and $\sigma_T = 0.1$ E for the Bouguer anomaly and gravity gradients, respectively. Although
257 these values are generally consistent with our data sets, they can exhibit local changes due to
258 various satellite elevations or relief variations, as well as data sources for the land
259 measurements. Here, to assess the relative contribution of σ_g and σ_T on our inversion results
260 we perform a systematic exploration of the role of the data uncertainties with $\sigma_g \in$
261 $[5 \text{ mGal}; 30 \text{ mGal}]$ and $\sigma_T \in [0.01 \text{ E}; 0.2 \text{ E}]$. We generate a normal distributed random noise with
262 a mean of zero and a standard deviation σ_g or σ_T , which is added to the synthetic data sets
263 calculated from the reference model with $\alpha_{west} = 25$ and $\alpha_{east} = 75$.

264 Unsurprisingly, our results on gravity and gravity gradients show that data dispersion can affect
265 the standard deviation of the obtained transition zone parameters: the lower the data
266 uncertainties, the lower the standard deviation on the model parameters (Figure 11). Our results
267 also suggest a greater dependence on the gravity gradient uncertainty than on Bouguer
268 anomaly uncertainty. Indeed, irrespective of the value of σ_g , the standard deviation on model
269 parameters is low if σ_T is small ($\sigma_T < 0.02 \text{ E}$). Besides, it can be noted that for the same σ_g and
270 σ_T , the obtained standard deviation differs from one parameter to another. The standard
271 deviation on α_{west} is low (< 7) compared to what is obtained for α_{east} (Figure 11a,b). The
272 location of the western boundary of the transition zone thus appears to be better constrained
273 than the eastern one. Likewise, figure 11c,d indicates that the standard deviation for the location
274 of the mid-profile is very low (< 4 ; corresponding to ca. 20 km), while for the width it can reach
275 more than 15 (about 75 km). This confirms our finding mentioned in the two previous
276 paragraphs suggesting that the inversion of gravity data sets gives better constraints on the
277 mid-profile location than on the lateral extent of the transition zone.

278 4. Application to the transition zone between the Nepal and Bhutan segments

279 In the previous section, our synthetic tests underlined the need to use jointly ground and
280 satellite gravity data. They demonstrated the robustness of our inversion approach and made it
281 possible to estimate its limitations. In the following, we apply this approach to characterize the
282 transition zone between the profiles of Nepal and Bhutan. Due to the lack of information
283 associated with heterogeneous ground gravity datasets and various satellite elevations, we
284 assume a standard deviation of 10 mGal and 0.1 E for the Bouguer anomaly and gravity
285 gradients, respectively.

286 4.1. Result

287 As the synthetic tests had shown, the T_{NW} component of satellite gravity gradients is not
288 relevant to constrain the geometry of the study transition zone (figure 12). Indeed, the obtained
289 normalized likelihood is relatively constant (between 0.7 and 1) and does not depend on the
290 assumed values of the coefficients α_{west} and α_{east} . On the contrary, the likelihood distributions
291 associated with the other gradients make it possible to better characterize the geometry of this
292 zone (figure 12). The inversion of T_{WW} and T_{WZ} gives quite similar likelihood distributions with a
293 α_{west} coefficient ranging between 60 and 75 and a α_{east} coefficient > 60 . The inversion of the
294 last component T_{ZZ} gives a more complex likelihood distribution. As for T_{WW} and T_{WZ} , it gives a
295 α_{east} coefficient greater than 60, but it also suggests three maxima: one with a very wide lateral
296 extension ($\alpha_{east} - \alpha_{west} > 70$ i.e a width > 350 km), one for which the western boundary is
297 located in easternmost Nepal ($\alpha_{west} \sim 70$), and the last one associated with a narrow transition
298 zone in western-central Bhutan located near Hammer's profile ($\alpha_{west} > 90$).

299 The inversion of the ground gravity dataset gives very similar results to those obtained for T_{ZZ}
300 (figure 12) with $\alpha_{west} > 50$ and with three maxima associated with the following coefficients
301 combinations ($\alpha_{west} \sim 20; \alpha_{east} \sim 95$), ($\alpha_{west} \sim 55; \alpha_{east} \sim 75$) and ($\alpha_{west} \sim 85; \alpha_{east} \sim 88$).

302 Compared to previous studies using Bouguer anomaly, the pattern of likelihood distribution is
303 consistent with the model of transition zone proposed by Hetényi et al. (2016) located on the
304 eastern border of Nepal, and that tentatively drawn by Godin and Harris (2014) through western
305 Bhutan.

306 The joint inversion of ground and satellite gravity data reduces the nonuniqueness of the gravity
307 inversion by limiting the range of α_{east} and by giving only one maximum for the calculated
308 likelihood. The best-fitting models ($L(m)_{g_z \text{ and } T_{ij}} > 0.6$) are obtained for α_{west} between 70 and
309 79 and α_{east} between 71 and 81 (figure 12). The best coefficients combination is ($\alpha_{west} =$
310 $76; \alpha_{east} = 78$), suggesting a very narrow (ca. 10 km wide) transition zone located between
311 Sikkim and the western border of Bhutan.

312 The calculated gravity field is in good agreement with the observations (figure 13). The
313 northward increase of Bouguer anomalies between the Ganga plain and the Tibetan plateau as
314 well as the lateral variations due to the curvature of the Himalayan arc are well explained by our
315 model. At shorter wavelengths, compared to the total signal the average difference between the
316 observed and calculated Bouguer anomaly along the Himalayan arc is low (<50 mGal)
317 suggesting that our models correctly also account for the latitudinal variations between Nepal
318 and Bhutan. Similarly, a good agreement is obtained for the GOCE gravity gradients. The main
319 features of the spatial distribution of gravity gradients are well-retrieved (figure 13). The average
320 residual is less than 0.2 E for T_{NW} and T_{ZZ} and reaches up to 0.3 E for T_{WW} and T_{WZ} .

321 It can be noted that our calculations slightly overestimate the amplitude of both the Bouguer
322 anomaly in central Tibet and the gravity gradients over the entire study area. This could suggest
323 that the density contrasts used in our models are too high, especially under the Tibetan plateau.
324 This could be corrected by changing either the crust-mantle density contrast or the extent of the
325 eclogitized lower crust. Such an approach would require a systematic study, which is however
326 beyond the scope of this paper. Moreover, this correction mainly concerns the northern part of

327 our study area, so it will not significantly modify our findings on the geometry of the transition
328 zone between the segments of Nepal and Bhutan.

329 At shorter wavelengths, our calculations cannot explain some local variations highlighted by
330 ground gravity data such as those observed in the Ganga plain near longitude 88°. This
331 inconsistency can be related to the approach itself. For the sake of simplicity, in our
332 calculations, we have only used six different densities associated with the sediment foreland
333 basin, the Tibetan crust, and the upper crust, the lower crust (eclogitized beneath Tibet) and the
334 lithospheric mantle of the Indian plate. No density variation within the same layer is therefore
335 taken into account and no local variations of the gravity field can be simulated.

336

337 **4.2. Discussion**

338 In the northern part of our study area, the 350 km long Pumqu-Xainza rift and the 500 km long
339 Yadong-Gulu rift are the two main tectonic features (figure 14). Located in southern and central
340 Tibet, they are already proposed as preexisting weak zones favoring the lithosphere tearing
341 (e.g. Chen et al., 2015; Li and Song, 2018). In southern Tibet, the location of the obtained
342 transition zone coincides with the southernmost part of Yadong-Gulu graben. Besides, its small
343 width and the steeper Indian plate in Bhutan compared to Nepal (figure 2) suggest a sub-vertical
344 east-dipping lateral ramp consistent with geological and geophysical observations across the
345 Yadong structure (e.g. Burchfield et al., 1992; Hauck et al., 1998; Zhang et al., 2013; Wang et
346 al., 2017). One can however note the difference in orientation between the obtained transition
347 zone and the NNE-SSW trending Yadong normal faults at the western border of Bhutan. This
348 disagreement is related to our approach itself, which is based on the lateral extension of
349 Berthet's section and Hammer's north-south profile and thus allows us to model solely radial
350 transition zones which are north-south trending in Bhutan. However, this limitation does not

351 significantly affect our result suggesting that the Yadong structure controls the segmentation in
352 southern Tibet.

353 In the Himalaya the location of the obtained transition also coincides with the northern part of
354 the Dhubri–Chunghang fault (DCF). This dextral fault zone has no geomorphological surface
355 expression but is well-constrained by a 20-40 km deep active dextral strike-slip seismicity (Diehl
356 et al., 2017). While the oblique orientation of the DCF cannot be taken into account in our
357 approach using radial profile, our results confirm the finding of Diehl et al. (2017) underlying the
358 key role of the DCF in the segmentation of the downgoing Indian plate.

359 The southern part of our study area consists of Himalayan foreland basins and Precambrian
360 metamorphic terrains constituting the Indian shield. In our approach, the lateral variation in the
361 depth of sedimentary basins is defined *a priori* (figure 2) and is also reflected in field data
362 (Dasgupta et al. 2000, reported in Hetényi et al. 2016 figure 4c). It cannot therefore be used to
363 discuss our results. On the contrary, no *a priori* information is given from the location of inherited
364 tectonic structures. They include the Munger-Saharsa ridge and the Shillong plateau visible in
365 the topography of northern India (figure 14). The often proposed linkage between the Yadong-
366 Gulu rift and the Munger-Saharsa ridge (e.g. Ni and Barazangi, 1984) suggests that this
367 structure has a key role in the segmentation of Himalaya. However, the obtained transition zone
368 does not coincide with this structure, as it is offset eastwards by > 50 km. Inherited tectonic
369 features also include approximately north-south trending structures as the Pingla and the
370 Kishanganj faults bounding the eastern edge of the Munger-Saharsa ridge, the blind Madhupur
371 fault (also named the Tista fault) in northern Bangladesh (Morgan and McIntire, 1959) and the
372 Dhubri fault located along the western edge of the Shillong Plateau (Figure 14). The obtained
373 transition zone is located between the Kishanganj and Madhupur active faults. It coincides with
374 the Madhupur fault in the southern edge of Himalaya, but considering the possible deviation in
375 its width (see synthetic tests figure 11) as well as its orientation limitation due to our approach,
376 the control of the Kishanganj fault cannot be ruled out. We still favor the most likely model, for

377 which the transition zone between the Nepal and Bhutan segments links the Madhupur fault and
378 the Dhubri–Chungthang fault with the Yadong rift. Recently, Dal Zilio et al. (2020) estimated the
379 spatial distribution of interseismic coupling along the Main Himalayan Thrust, which is the
380 megathrust accommodating most of the shortening across the Himalayan range. In our study
381 area, they obtained a heterogeneous distribution, for which fault patches with low interseismic
382 coupling in eastern Nepal coincide with the Munger-Saharsa ridge. Further east, this coupling
383 remains low until the longitude of the obtained transition zone where we can observe an abrupt
384 increase in coupling consistent with geodetic data in western Bhutan (Marechal et al., 2016).
385 This spatial coincidence strengthens our findings by suggesting the relationship between
386 interseismic coupling zonation and the segmentation of the Himalayan arc proposed by Dal Zilio
387 et al. (2020).

388 Due to uncertainties in dating past seismic events (which can be several hundred years old),
389 paleoseismic studies performed in our area suggest the occurrence of either (1) a sequence of
390 great $M > 8$ earthquakes between 1020 and 1520 or (2) a giant earthquake in ca. 1100 which
391 broke more than 700 km distance along the Himalayan arc between central Nepal and eastern
392 Bhutan (figure 14). Our approach partly allows us to resolve this question. We obtain an abrupt
393 and narrow transition located near the western boundary of Bhutan. Such a sub-vertical lateral
394 ramp could act as a barrier to earthquake rupture propagation and thus could restrict the extent
395 of major earthquakes to only one side and therefore a shorter seismic segment. This favors the
396 first scenario presented above, for which the observations between Nepal and Bhutan on either
397 side of the transition zone are unlikely to be linked to the same seismic event. In that case, the
398 paleoseismic studies performed in easternmost Nepal by Nakata et al. (1998), Upreti et al.
399 (2000), and Wesnousky et al. (2017b) can provide key information on the termination of the
400 rupture that affected Nepal in ca. 1100. While this hypothesis remains speculative, it is
401 supported by the low interseismic coupling obtained in this area by Dal Zilio et al. (2020), which
402 leads to a small accumulation of stress to be released during a forthcoming earthquake.

403 Constraints on the location of the M8 earthquake in 1714 in Bhutan (Hetényi et al. 2016b) are
404 also coherent with the transition zone found in this study.

405 **5. Conclusions**

406 Taking advantage of the available information in Nepal and Bhutan, we have developed an
407 inversion approach to explore the along-arc segmentation of the Himalayan belt using mainly
408 gravity data. Synthetic tests demonstrate the effectiveness of the approach to locate the two
409 edges of the transition zone between the segments of the central and the eastern Himalaya.
410 Irrespective of the location along the Himalayan arc and the lateral extent of this transition zone,
411 these two parameters are found with a standard deviation $< 0.2^\circ$ longitude along the MFT and
412 ca. 35 km in width. Synthetic tests also underline the need for joint inversion of both Bouguer
413 anomaly measurements and GOCE gravity gradient observations to reduce the nonuniqueness
414 of gravity inversions.

415 The joint inversion of ground and satellite data sets suggest a ca. 10 km wide transition zone
416 located at the western border of Bhutan. Compared to previous studies using Bouguer anomaly
417 only, this transverse tectonic feature is between the location proposed by Hetényi et al. (2016)
418 on the eastern border of Nepal, and that proposed by Godin and Harris (2014) through western
419 Bhutan. This abrupt segmentation is supported by structural observations and could be related
420 to the Madhupur fault in the foreland, the Dhubri–Chungthang fault cutting the India plate
421 beneath Himalaya and the Yadong-Gulu rift in southern Tibet.

422 The obtained transition zone is narrow enough to possibly prevent seismic rupture propagation
423 across this boundary between Nepal and Bhutan. This could result in the seismic segmentation
424 of the Main Himalayan Thrust and potentially restrict the size of large earthquakes along the
425 Himalayan belt. Such information are essential inputs of seismic hazard models, as they delimit
426 the extent of possible fault sources. The more precise location, geometry and nature of this and

427 other transitions in the Himalaya – whether it is a ramp, a fault, or other feature, – should be
428 investigated in the future. Forthcoming research will hence contribute to improve existing
429 probabilistic seismic hazard models of Northern India, Nepal (Stevens et al. 2018) and Bhutan
430 (Stevens et al. 2020).

431 Acknowledgments.

432 The authors acknowledge the comments and helpful suggestions of the editor Sebastiano
433 D’Amico and two anonymous reviewers that helped to improve the manuscript. This work was
434 supported by grants from the Agence National de la Recherche ANR-18-CE01-0017 and CNES
435 TOSCA, as well as the Swiss National Science Foundation grant PP00P2_157627 (project
436 OROG3NY). The figures of this paper were prepared using the Generic Mapping Tools version
437 6 (Wessel et al., 2019).

438 **Reference**

439 Banerjee, P. (1998). Gravity measurements and terrain corrections using a digital terrain
440 model in the NW Himalaya. *Comp. Geosci.* 24, 1009–1020.

441 Berthet, T., Hetényi, G., Cattin, R. , Sapkota, S.N., Champollion, C., Kandel, T., Doerflinger,
442 E., Drukpa, D., Lechmann, S., and Bonin, M. (2013). Lateral similarity of India plate strength
443 and crustal structure over Central and Eastern Nepal, *Geophys. J.Int.*, 195, 1481–1493, doi :
444 10.1093/gji/ggt357.

445 Bollinger, L., Sapkota, S. N., Tapponnier, P., Klinger, Y., Rizza, M., Van Der Woerd, J.,
446 Tiwari, D.R., Pandey, R., Bitri, A. and Bes de Berc, S. (2014). Estimating the return times of
447 great Himalayan earthquakes in eastern Nepal: Evidence from the Patu and Bardibas strands of
448 the Main Frontal Thrust. *Journal of Geophysical Research: Solid Earth*, 119(9), 7123-7163.

449 Burchfiel, B. C., Zhiliang, C., Hodges, K. V., Yuping, L., Royden, L. H., and Changrong, D.
450 (1992). The South Tibetan detachment system, Himalayan orogen: Extension contemporaneous

451 with and parallel to shortening in a collisional mountain belt (Vol. 269). Geological Society of
452 America.

453 Cattin, R., Mazzotti, S., & Baratin, L. M. (2015). GravProcess: An easy-to-use MATLAB
454 software to process campaign gravity data and evaluate the associated uncertainties.
455 Computers & geosciences, 81, 20-27.

456 Chen, Y., Li, W., Yuan, X., Badal, J., and Teng, J. (2015). Tearing of the Indian lithospheric
457 slab beneath southern Tibet revealed by SKS-wave splitting measurements. Earth and
458 Planetary Science Letters, 413, 13-24.

459 Coutand, I., D. M. Whipp Jr., D. Grujic, M. Bernet, M. G. Fellin, B. Bookhagen, K. R. Landry,
460 S. K. Ghalley, and C. Duncan (2014), Geometry and kinematics of the Main Himalayan Thrust
461 and Neogene crustal exhumation in the Bhutanese Himalaya derived from inversion of
462 multithermochronologic data, J. Geophys. Res. Solid Earth, 119, 1446–1481,
463 doi:10.1002/2013JB010891.

464 Dal Zilio, L., Jolivet, R., and van Dinther, Y. (2020). Segmentation of the Main Himalayan
465 Thrust illuminated by Bayesian inference of interseismic coupling. Geophysical Research
466 Letters, 47, e2019GL086424.

467 Das, D., Mehra, G., Rao, K. G. C., Roy, A. L. and Narayana, M. S. (1979). Bouguer, free-air
468 and magnetic anomalies over northwestern Himalaya. Himalayan Geology seminar, Section III,
469 Oil and Natural Gas Resources. Geol. Surv. India Misc. Publ. 41, 141–148.

470 Dasgupta, S. et al. (2000). Seismotectonic Atlas of India and its environs (eds Narula, P. L.,
471 Acharyya, S. K. & Banerjee J.) 87 pp (Geological Survey of India, Calcutta, India.

472 Diehl, T., Singer, J., Hetényi, G., Grujic, D., Clinton, J., Giardini, D., Kissling, E. and
473 GANSSER Working Group. (2017). Seismotectonics of Bhutan: Evidence for segmentation of
474 the Eastern Himalayas and link to foreland deformation. Earth and Planetary Science Letters,
475 471, 54-64.

476 Duncan, C., Masek, J., and Fielding, E. (2003). How steep are the Himalaya?
477 Characteristics and implications of along-strike topographic variations, *Geology*, 31, 75-78,
478 doi:10.1130/0091-7613.

479 Fuchs, M. and Bouman, J. (2011). Rotation of GOCE gravity gradients to local frames.
480 *Geophys. J. Int.* 187, 743-753 .

481 Godin, L., and Harris, L. B. (2014). Tracking basement cross-strike discontinuities in the
482 Indian crust beneath the Himalayan orogen using gravity data—relationship to upper crustal
483 faults. *Geophysical Journal International*, 198(1), 198-215.

484 Gahalaut, V.K., Arora, B.R. (2012). Segmentation of seismicity along the Himalayan Arc due
485 to structural heterogeneities in the under-thrusting Indian plate and overriding Himalayan
486 wedge, *Episodes*, 35, 4, 493-500.

487 Gruber, T., Visser, P. N., Ackermann, C., and Hosse, M. (2011). Validation of GOCE gravity
488 field models by means of orbit residuals and geoid comparisons. *Journal of Geodesy*.

489 Hammer, P., Berthet, T., Hetényi, G., Cattin, R., Drukpa, D., Chopel, J., Lechmann, S.,
490 Moigne, N.L., Champollion, C. and Doerflinger, E. (2013). Flexure of the India plate underneath
491 the Bhutan Himalaya. *Geophysical research letters*, 40(16), pp.4225-4230.

492 Hauck, M. L., Nelson, K. D., Brown, L. D., Zhao, W., and Ross, A. R. (1998). Crustal
493 structure of the Himalayan orogen at ~ 90 east longitude from Project INDEPTH deep reflection
494 profiles. *Tectonics*, 17(4), 481-500.

495 Hetényi G, Cattin R, Brunet F, Vergne J, Bollinger L, Nábělek JL, Diament M (2007) Density
496 distribution of the India plate beneath the Tibetan Plateau: geophysical and petrological
497 constraints on the kinetics of lower-crustal eclogitization. *Earth Planet Sci Lett* 264:226-244.
498 doi:10.1016/j.epsl.2007.09.036.

499 Hetényi, G., Cattin, R., Berthet, T., Le Moigne, N., Chopel, J., Lechmann, S., Hammer, P.,
500 Drukpa, D., Sapkota, S.N., Gautier, S. and Thinley, K. (2016). Segmentation of the Himalayas
501 as revealed by arc-parallel gravity anomalies. *Scientific reports*, 6(1), 1-10.

502 Hetényi G, Le Roux-Mallouf R, Berthet T, Cattin R, Cauzzi C, Phuntsho K, Grolimund R
503 (2016b) Joint approach combining damage and paleoseismology observations constrains the
504 1714 A.D. Bhutan earthquake at magnitude 8 ± 0.5 . *Geophys Res Lett* **43**:10695-10702.
505 doi:10.1002/2016GL071033

506 Kumar, S., Wesnousky, S. G., Jayangondaperumal, R., Nakata, T., Kumahara, Y., and
507 Singh, V., (2010). Paleoseismological evidence of surface faulting along the northeastern
508 Himalayan front, India: Timing, size, and spatial extent of great earthquakes, *J. Geophys. Res.*,
509 115(B12), B12422.

510 Lavé, J., Yule, D., Sapkota, S., Basant, K., Madden, C., Attal, M., and Pandey, R. (2005).
511 Evidence for a great Medieval earthquake (~ 1100 AD) in the central Himalayas, Nepal.
512 *Science*, 307(5713), 1302-1305.

513 Le Roux-Mallouf, R., Godard, V., Cattin, R., Ferry, M., Gyeltshen, J., Ritz, J.F., Drukpa, D.,
514 Guillou, V., Arnold, M., Aumaître, G. and Bourlès, D.L. (2015). Evidence for a wide and gently
515 dipping Main Himalayan Thrust in western Bhutan. *Geophysical research letters*, 42(9), 3257-
516 3265.

517 Le Roux-Mallouf, R., Ferry, M., Ritz, J.-F., Berthet, T., Cattin, R., and Drukpa, D. (2016).
518 First paleoseismic evidence for great surface-rupturing earthquakes in the Bhutan Himalayas, *J.*
519 *Geophys. Res. Solid Earth*, 121, doi:10.1002/2015JB012733.

520 Le Roux-Mallouf, R., Ferry, M., Cattin, R., Ritz, J. F., Drukpa, D., and Pelgay, P. (2020). A
521 2600-yr-long paleoseismic record for the Himalayan Main Frontal Thrust (Western Bhutan).
522 *Solid Earth*, 11, 2359-2375.

523 Le Fort, P. (1975). Himalaya: the collided range. Present knowledge of the continental arc.,
524 *Am. J. Sci.*, 275A, 1–44.

525 Li, J., and Song, X. (2018). Tearing of Indian mantle lithosphere from high-resolution seismic
526 images and its implications for lithosphere coupling in southern Tibet. *Proceedings of the*
527 *National Academy of Sciences*, 115(33), 8296-8300.

528 Marechal, A., Mazzotti, S., Cattin, R., Cazes, G., Vernant, P., Drukpa, D., Trinley, K.,
529 Tarayoun, A., Le Roux-Mallouf, R., Thapa, BB., Pelgay, P., Gyeltshen, J., Doerflinger, E and
530 Gautier, S. (2016). Evidence of interseismic coupling variations along the Bhutan Himalayan arc
531 from new GPS data. *Geophysical Research Letters*, 43(24), 12-399.

532 Martelet, G., Sailhac, P., Moreau, F. and Diament, M. (2001). Characterization of geological
533 boundaries using 1-D wavelet transform on gravity data: theory and application to the
534 Himalayas. *Geophysics* 66, 1116–1129.

535 McQuarrie, N., Robinson, D., Long, S., Tobgay, T., Grujic, D., Gehrels, G., and Ducea, M.
536 (2008), Preliminary stratigraphic and structural architecture of Bhutan: Implications for the along
537 strike architecture of the Himalayan system: *Earth and Planetary Science Letters*, 272, p. 105-
538 117, doi: 10.1016/j.epsl.2008.04.030.

539 McQuarrie, N., and T. A. Ehlers (2015), Influence of thrust belt geometry and shortening rate
540 on thermochronometer cooling ages: Insights from thermokinematic and erosion modeling of the
541 Bhutan Himalaya, *Tectonics*, 34,1055–1079, doi:10.1002/2014TC003783.

542 Morgan, J. P., and McIntire, W. G. (1959). Quaternary geology of the Bengal basin, East
543 Pakistan and India. *Geological Society of America Bulletin*, 70(3), 319-342.

544 Mugnier, J.-L., Gajurel, A., Huyghe, P., Jayangandaperumal, R., Jouanne, F. and Upreti, B.
545 (2013). Structural interpretation of the great earthquakes of the last millennium in the central
546 Himalaya, *Earth Science Reviews*, doi: 10.1016/j.earscirev.2013.09.003.

547 Nábělek, J., Hetényi, G., Vergne, J., Sapkota, S., Kafle, B.,Jiang, M., Su, H., Chen, J., and
548 Huang, B.S. (2009). Underplating in the Himalaya-Tibet collision zone revealed by the Hi-CLIMB
549 experiment, *Science*, 325(5946), pp.1371-1374.

550 Nakata, T., Kumura, K. and Rockwell, T. (1998), First successful paleoseismic trench study
551 on active faults in the Himalaya, *Eos Trans. AGU*, 79, 45.

552 Ni, J., and Barazangi, M. (1984). Seismotectonics of the Himalayan collision zone:
553 Geometry of the underthrusting Indian plate beneath the Himalaya. *Journal of Geophysical*
554 *Research: Solid Earth*, 89(B2), 1147-1163.

555 Rajendran, C. P., John, B., and Rajendran, K. (2015). Medieval pulse of great earthquakes
556 in the central Himalaya: Viewing past activities on the frontal thrust. *Journal of Geophysical*
557 *Research: Solid Earth*, 120(3), 1623-1641.

558 Robert, X., Van Der Beek, P., Braun, J., Perry, C., and Mugnier, J.-L. (2011). Control of
559 detachment geometry on lateral variations in exhumation rates in the Himalaya: Insights from
560 low-temperature thermochronology and numerical modeling, *J. Geophys. Res.*, 116, B05202,
561 doi:10.1029/2010JB007893.

562 Sapkota, S. N., Bollinger, L., Klinger, Y., Tapponnier, P., Gaudemer, Y., and Tiwari, D.
563 (2013). Primary surface ruptures of the great Himalayan earthquakes in 1934 and 1255. *Nature*
564 *Geoscience*, 6(1), 71-76.

565 Saraswati, A. T., Cattin, R., Mazzotti, S. and Cadio, C. (2019). New analytical solution and
566 associated software for computing full-tensor gravitational field due to irregularly shaped bodies.
567 *Journal of Geodesy*, 93(12), 2481-2497.

568 Schulte-Pelkum, V., Monsalve, G., Sheehan, A., Pandey, M. R., Sapkota, S., Bilham, R., &
569 Wu, F. (2005). Imaging the Indian subcontinent beneath the Himalaya. *Nature*, 435(7046),
570 1222-1225.

571 Singer, J., Kissling, E., Diehl, T., and Hetényi, G. (2017). The underthrusting Indian crust
572 and its role in collision dynamics of the Eastern Himalaya in Bhutan: Insights from receiver
573 function imaging, *J. Geophys. Res. Solid Earth*, 122, 1152–1178, doi:10.1002/2016JB013337.

574 Stevens, V. L., Shrestha, S. N., & Maharjan, D. K. (2018). Probabilistic Seismic Hazard
575 Assessment of Nepal. *Bulletin of the Seismological Society of America*, 108(6), 3488-3510.

576 Stevens, V. L., De Risi, R., Le Roux-Mallouf, R., Drukpa, D., and Hetényi, G. (2020).
577 Seismic hazard and risk in Bhutan. *Natural Hazards*, 104(3), 2339-2367.

578 Sun, W. (1989). Bouguer Gravity Anomaly Map of the People's Republic of China. Chin.
579 Acad. Geoexploration, Beijing.

580 Tiwari, V. M., Vyghreswara, R., Mishra, D. C. and Singh, B. (2006). Crustal structure across
581 Sikkim, NE Himalaya from new gravity and magnetic data. *Earth Planet. Sci. Lett.* 247, 61–69.

582 Upreti, B.N., Nakata, T., Kumahara, Y., Yagi, H., Okumura, K., Rockwell, T.K. and Viridi,
583 N.S. (2000). The latest active faulting in Southeast Nepal. In: *Proceedings of the Hokudan*
584 *International Symposium and School in Active Faulting, Awaji Island, Hyogo Japan*, 533–536.

585 Wang, G., Wei, W., Ye, G., Jin, S., Jing, J., Zhang, L., Dong, H., Xie, C., Omisore, B.O. and
586 Guo, Z. (2017). 3-D electrical structure across the Yadong-Gulu rift revealed by magnetotelluric
587 data: new insights on the extension of the upper crust and the geometry of the underthrusting
588 Indian lithospheric slab in southern Tibet. *Earth and Planetary Science Letters*, 474, 172-179.

589 Wesnousky, S.G., Kumahara, Y., Chamlagain, D., Pierce, I.K., Karki, A. and Gautam, D.
590 (2017a). Geological observations on large earthquakes along the Himalayan frontal fault near
591 Kathmandu, Nepal. *Earth Planet. Sci. Lett.* 457, 366–375.

592 Wesnousky, S.G., Kumahara, Y., Chamlagain, D., Pierce, I.K., Reedy, T., Angster, S.J. and
593 Giri, B. (2017b). Large paleoearthquake timing and displacement near Damak in eastern Nepal
594 on the Himalayan Frontal Thrust. *Geophys. Res. Lett.* 44, 8219–8226.

595 Wesnousky, S.G., Kumahara, Y., Nakata, T., Chamlagain, D. and Neupane, P. (2018). New
596 observations disagree with previous interpretations of surface rupture along the himalayan
597 frontal thrust during the great 1934 Bihar-Nepal Earthquake. *Geophys. Res. Lett.* 45, 2652–
598 2658.

599 Wesnousky, S. G., Kumahara, Y., Chamlagain, D., and Neupane, P. C. (2019). Large
600 Himalayan Frontal Thrust paleoearthquake at Khayarmara in Eastern Nepal. *Journal of Asian*
601 *Earth Sciences*, 174, 346-351.

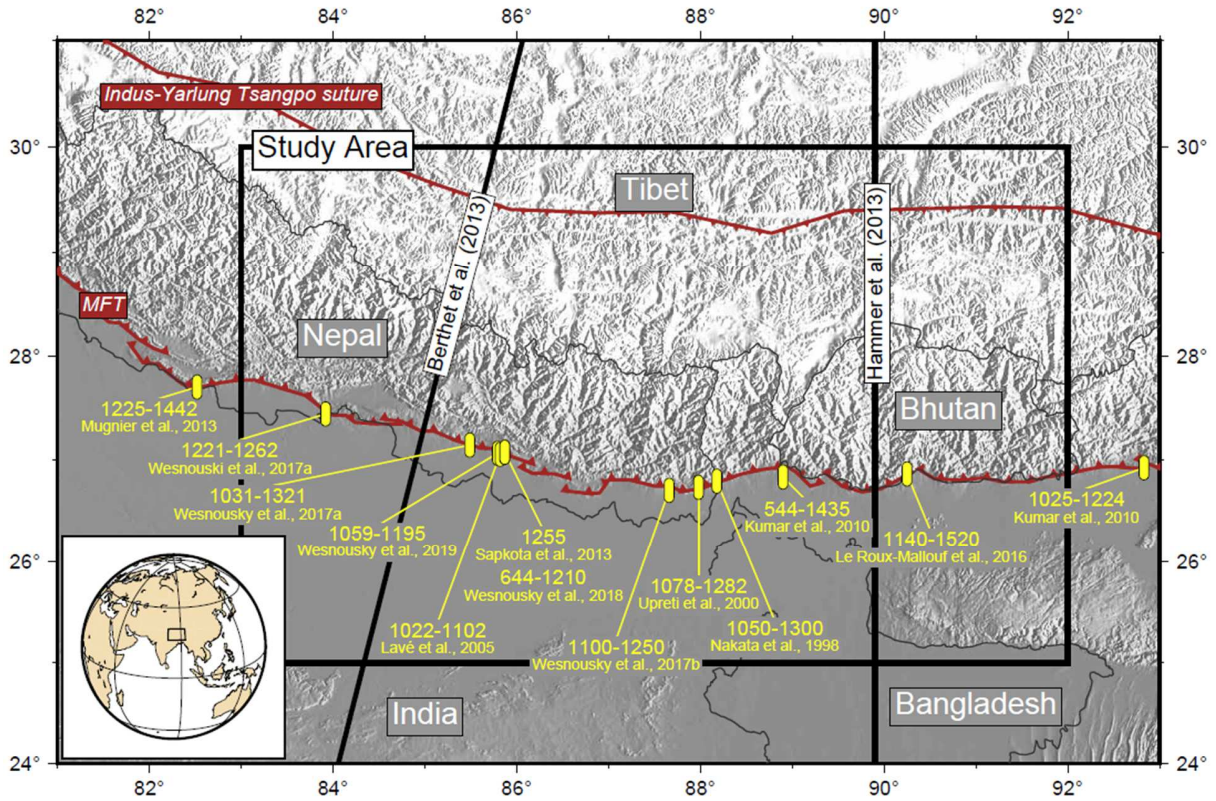
602 Wessel, P., Luis, J. F., Uieda, L., Scharroo, R., Wobbe, F., Smith, W. H. F., & Tian, D.
603 (2019). The generic mapping tools version 6. *Geochemistry, Geophysics, Geosystems*.

604 Zhang, Z., Chen, Y., Yuan, X., Tian, X., Klemperer, S. L., Xu, T., Bai, Z., Zhang, H., WU, J.
605 and Teng, J. (2013). Normal faulting from simple shear rifting in South Tibet, using evidence
606 from passive seismic profiling across the Yadong-Gulu Rift. *Tectonophysics*, 606, 178-186.
607

608 **Figure**

609

610



611

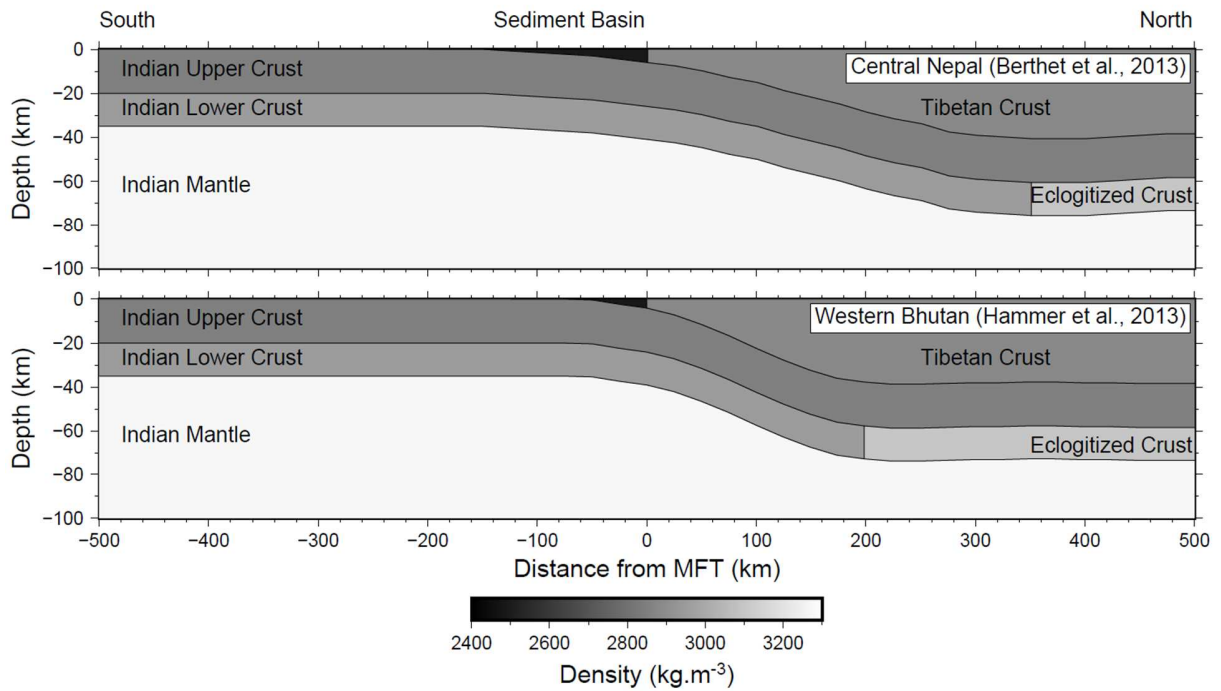
612 **Figure 1**

613 Elevation map of the Himalayas and surrounding regions. Yellow rectangles give the location of
614 medieval earthquake study sites along the Main Frontal Thrust (MFT) modified from Wesnousky
615 et al. (2019). Sites are labeled to show the age of paleoearthquakes and authors reporting
616 results. Black contour is the limit of our study area. Boundaries of India, Bangladesh, Nepal,
617 Bhutan, and Tibet as well as major tectonic structures (MFT and Indus-Yarlung Tsangpo suture)
618 are shown as reference. Black lines show the locations of profiles studied by Berthet et al.
619 (2013) and Hammer et al. (2013).

620

621

622
623

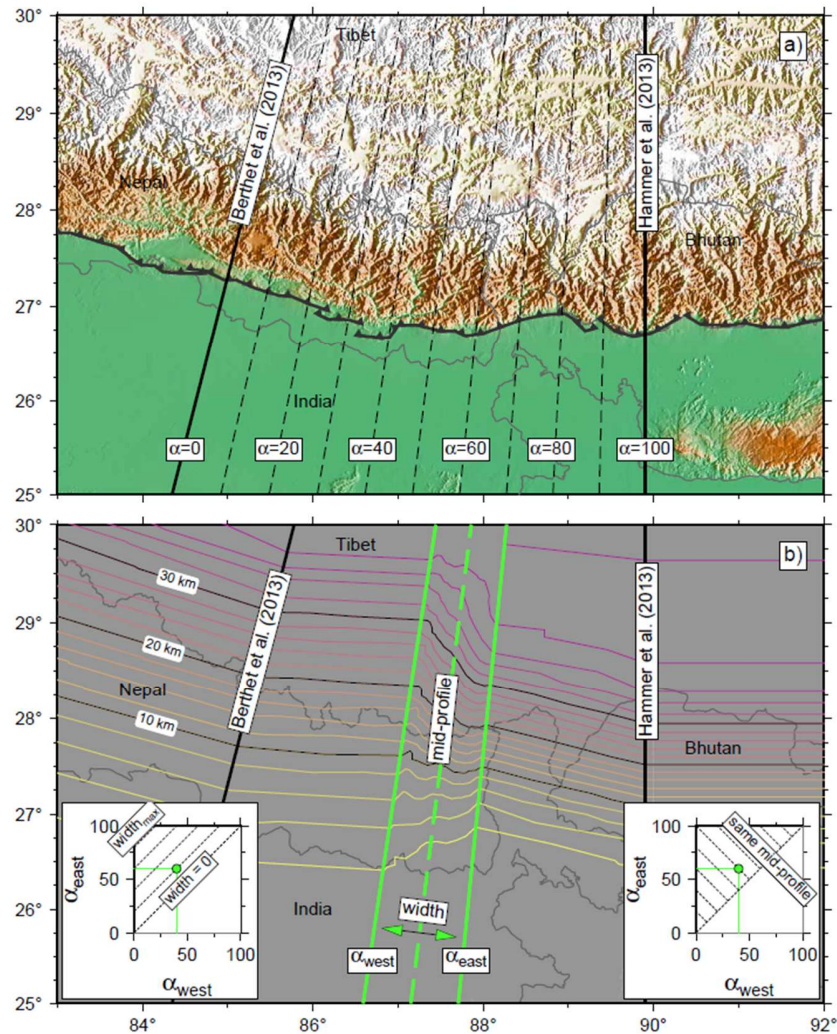


624

625 Figure 2

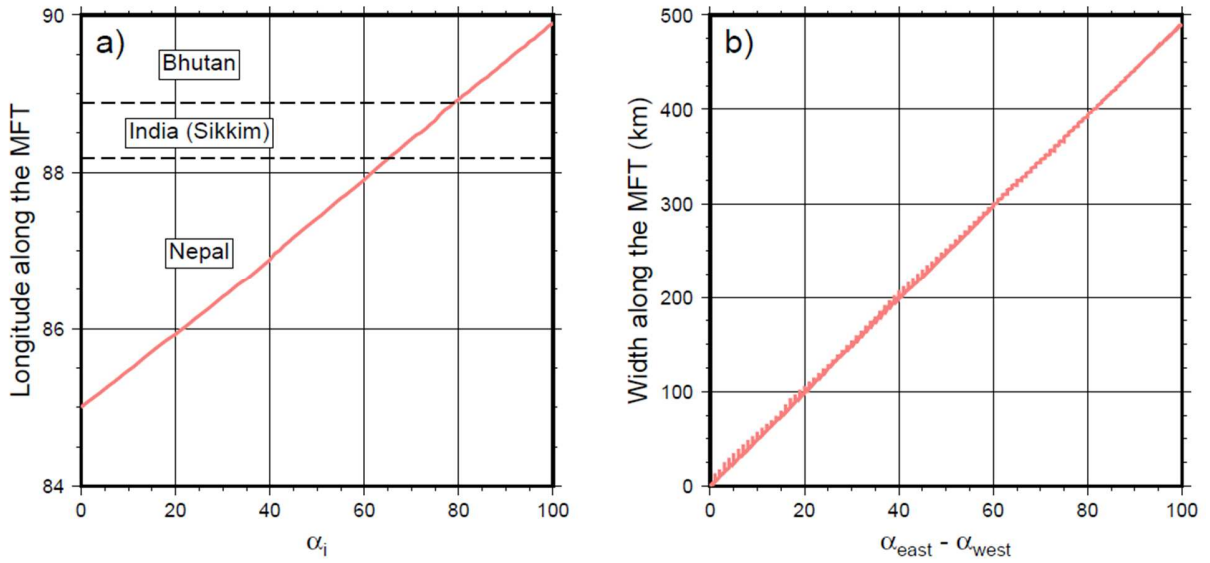
626 Geometry and density structure of the lithosphere in central Nepal and western Bhutan (see
627 location figure 1). These two profiles are inferred from Bouguer anomalies, receiver functions,
628 and boreholes data acquired across the Himalaya from India to Tibet (Berthet et al., 2013;
629 Hammer et al., 2013). They include sediment basin, Tibetan crust, and Indian plate, which is
630 composed of three layers: upper crust, lower crust (eclogitized beneath Tibet), and lithospheric
631 mantle.

632



635 Figure 3

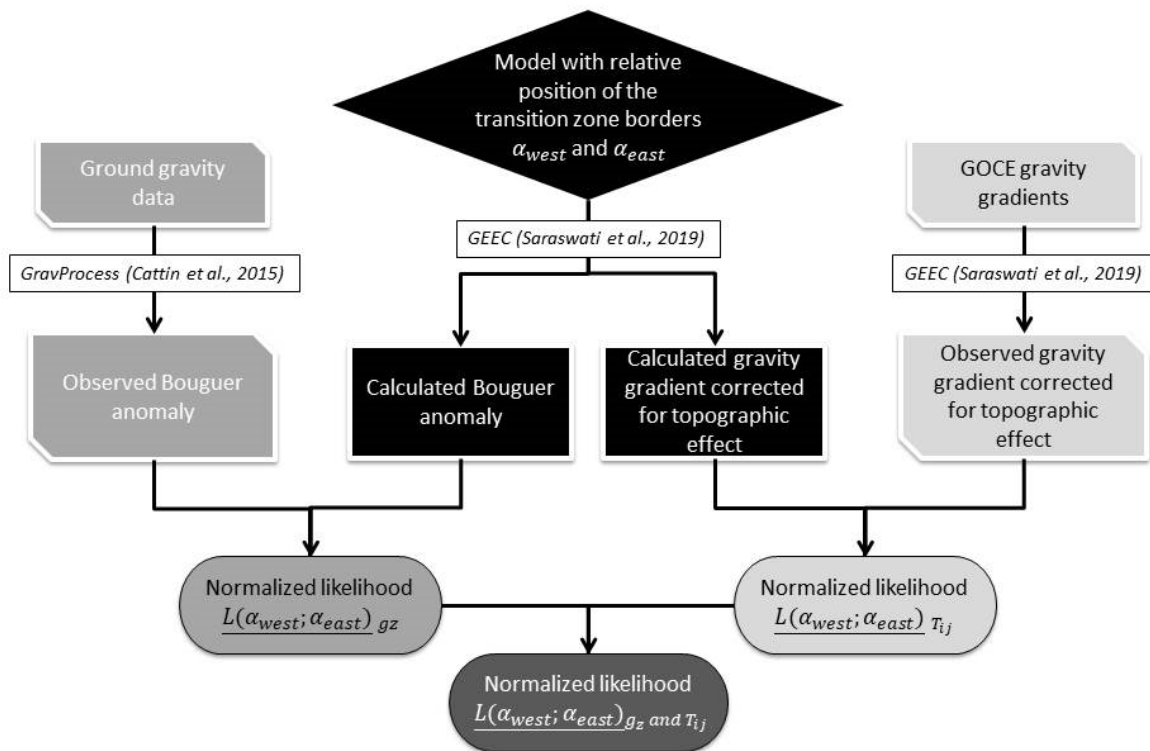
636 Method adopted to investigate the lateral variation of lithospheric structures between central
 637 Nepal and western Bhutan. (a) Topographic map showing the location of considered profiles. α
 638 is a weighting coefficient between the two previously studied profiles of central Nepal and
 639 western Bhutan. $\alpha = 0$ and $\alpha = 100$ are associated with the profile of Berthet et al. (2013) and
 640 Hammer et al. (2013), respectively. (b) Color contours show the modelled depth of the top of the
 641 downgoing Indian upper crust, which is defined from the two profiles depicted in figure 2 and
 642 from the transition zone bound by $\alpha_{west} = 40$ and $\alpha_{east} = 60$ (green lines). Left inset: Dashed
 643 lines parallel to the first bisector ($\alpha_{east} - \alpha_{west} = \text{constant}$) are associated with transition zones
 644 of similar width. Right inset: Dashed lines perpendicular to the first bisector represent transition
 645 zones with a similar mid-profile location ($[\alpha_{east} + \alpha_{west}]/2 = \text{constant}$).
 646



647
648

Figure 4

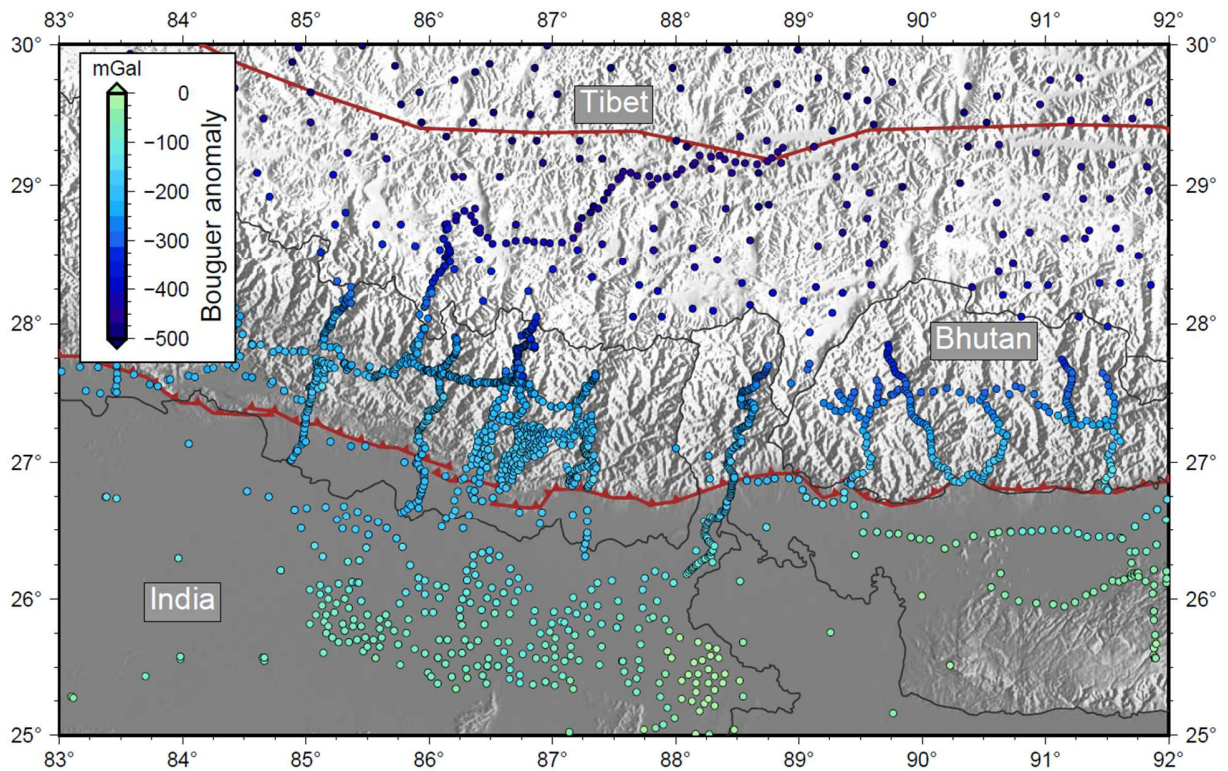
649 Relationship between the assumed coefficient α and the main features of the tested transition
 650 zone. (a) Geographic location of the study profiles given by their longitude along the Main
 651 Frontal Thrust (MFT). α_i refers either to α_{east} , α_{west} or $\alpha_{mid-profile} = [\alpha_{west} + \alpha_{east}]/2$. (b)
 652 Width of the transition zone along the MFT. Distances are obtained assuming that the points lie
 653 on the WGS84 reference ellipsoid.
 654



655

656 Figure 5

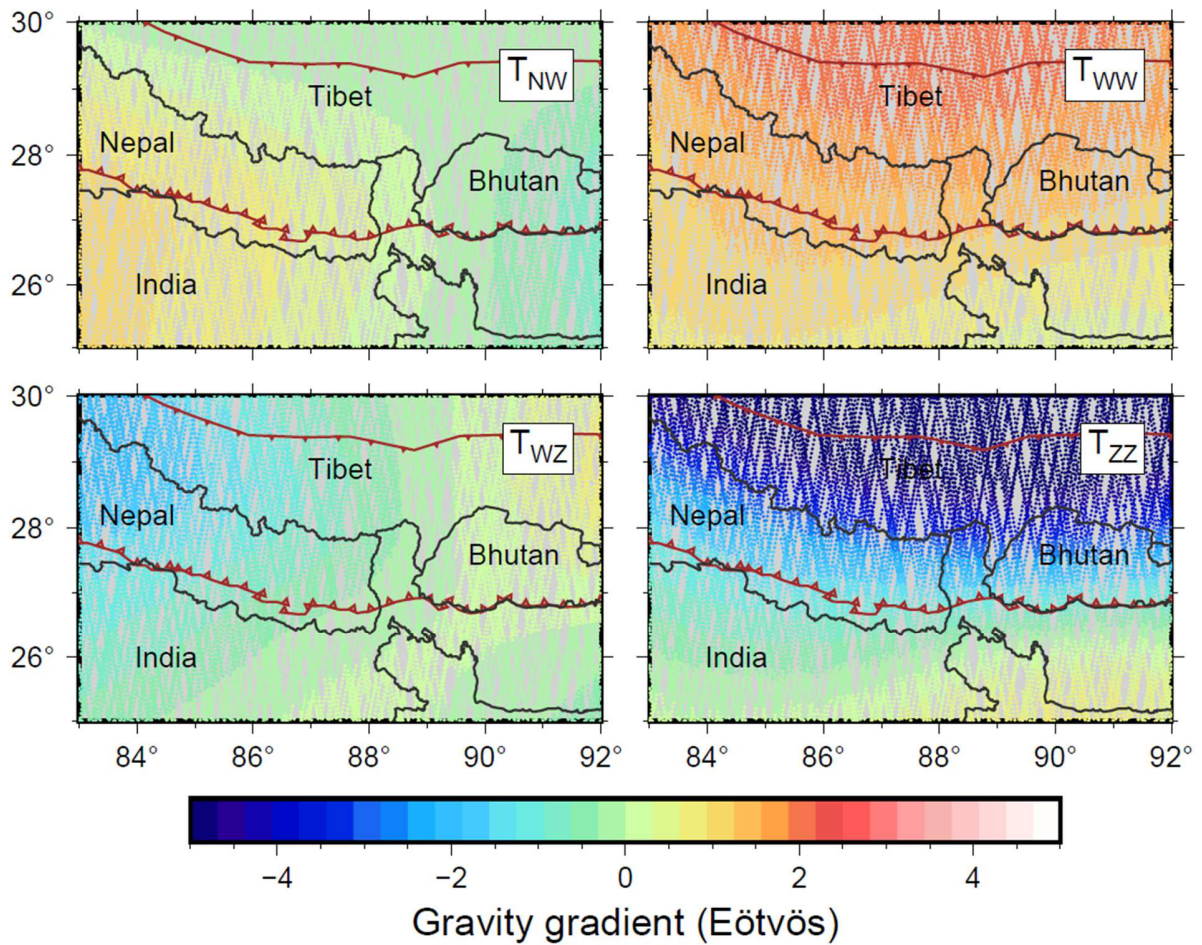
657 Flow chart for both data processing and models likelihood calculation. Ground gravity data are
 658 fully processed using the GravProcess software (Cattin et al., 2015) to obtain Bouguer anomaly.
 659 GOCE data reduction (topographic effect) is performed using the GEEC software with WGS84
 660 as the reference ellipsoid (Saraswati et al., 2019). We define a model geometry for the study
 661 transition zone using coefficients α_{west} and α_{east} for the relative position of its western and
 662 eastern boundaries (see figure 3). The associated likelihood is obtained from the comparison
 663 between the calculated and the observed Bouguer anomaly or gravity gradients and ultimately
 664 both. The inversion is then performed with a systematic exploration of the coefficients α_{west} and
 665 α_{east} in a range between 0 and 100 with a step of 1.
 666



667

668 Figure 6

669 Bouguer anomaly map of the Himalayas and surrounding regions. Color circles are associated
 670 with the gravity dataset compiled by Hetényi et al. (2016) from the International Gravimetric
 671 Bureau database (BGI, <http://bgi.omp.obs-mip.fr/>) and previous studies (Das et al., 1979; Sun,
 672 1989; Banerjee, 1998; Cattin et al., 2001; Tiwari et al., 2006; Hammer et al., 2013; Berthet et al.,
 673 2013). Boundaries of countries, geographic regions and the main tectonic structures are shown
 674 as reference.

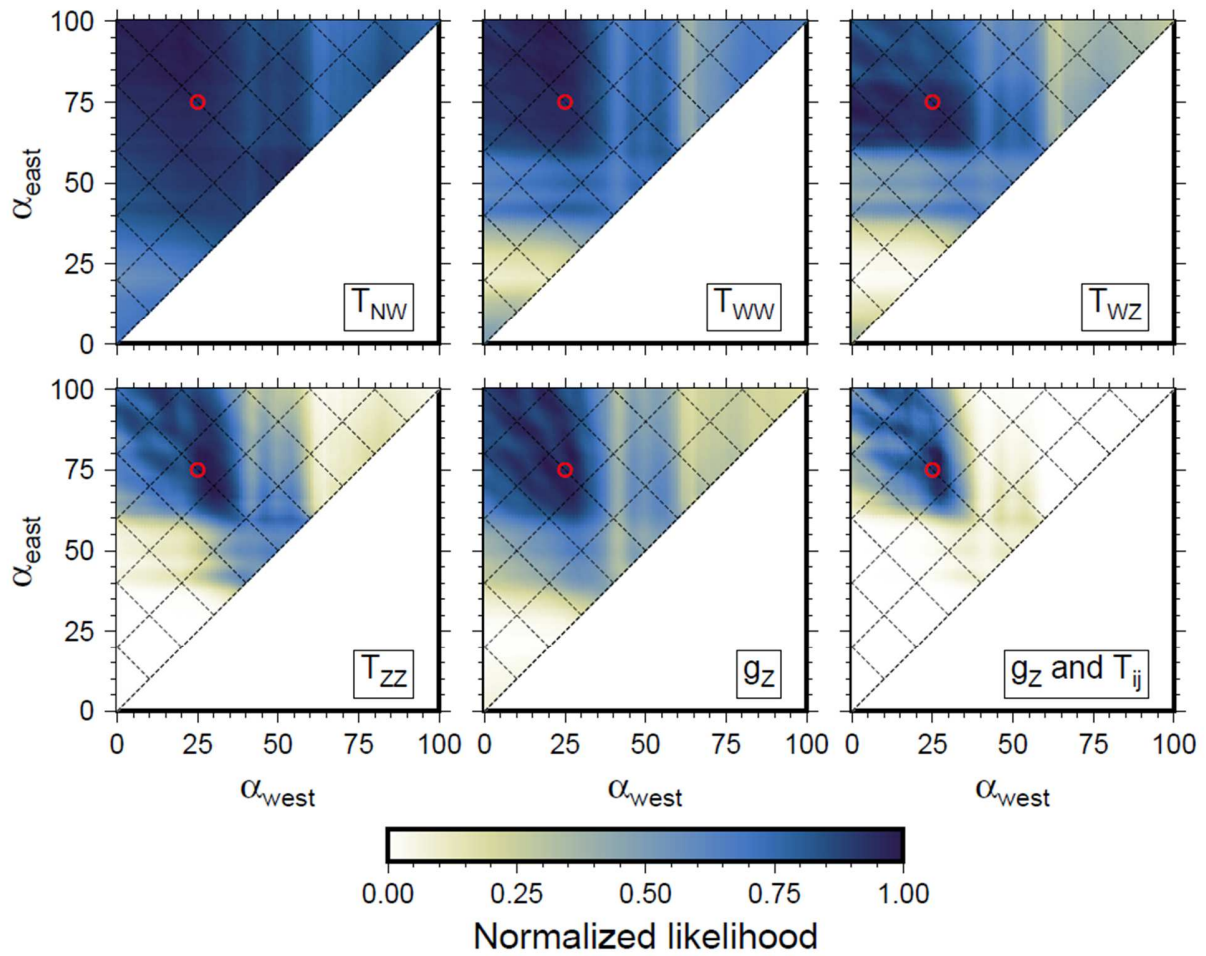


675

676 Figure 7

677 Map of gravity gradients including topographic corrections from the spatial gravity mission
 678 GOCE (Gravity Field and Steady-State Ocean Circulation Explorer). Color dots represent data
 679 along the satellite orbits at an altitude between 225 km and 265 km. T_{ij} is the ij component of
 680 gravity gradient tensor. T_{NW} , T_{WW} , and T_{WZ} are associated with the partial derivative of the three
 681 gravity components in the west direction. T_{ZZ} is the partial derivative of g_z in the vertical
 682 direction. Borders of countries and the main tectonic structures are shown as reference.

683

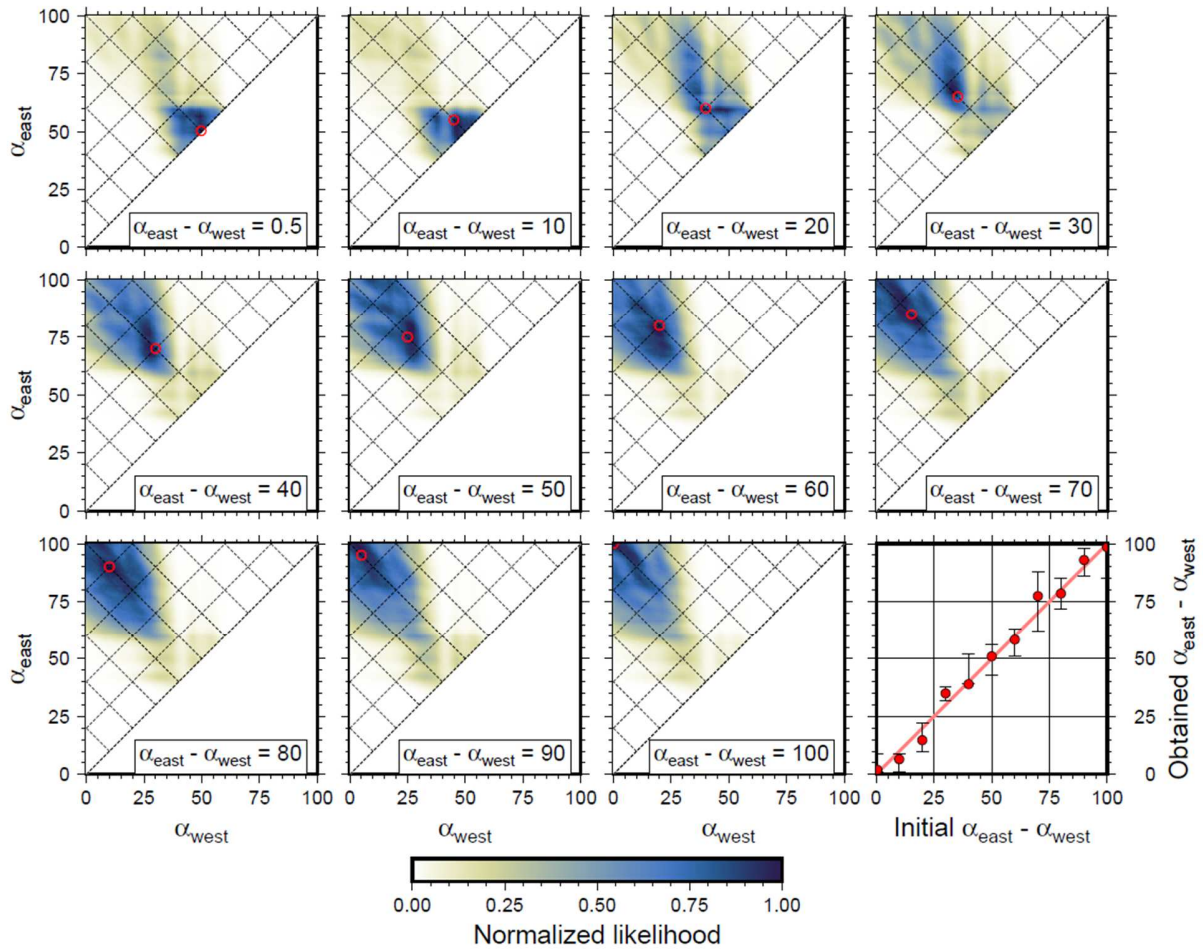


684

685 Figure 8

686 Synthetic test on gravity and gravity gradients assuming $\alpha_{west} = 25$ and $\alpha_{east} = 75$ as initial
687 coefficients (red circle). The color scale shows for all tested α_{west} and α_{east} values the
688 calculated likelihood obtained either from gravity gradient (T_{NW} , T_{WW} , T_{WZ} and T_{ZZ}), from
689 Bouguer anomaly (g_Z) or from all (g_Z and T_{ij}). This likelihood distribution is normalized with
690 respect to the best-fitting model obtained for each considered dataset. $\sigma_g = 10 \text{ mGal}$ and $\sigma_T =$
691 $0.1 E$ are assumed for the standard deviations of gravity and gravity gradient data, respectively.

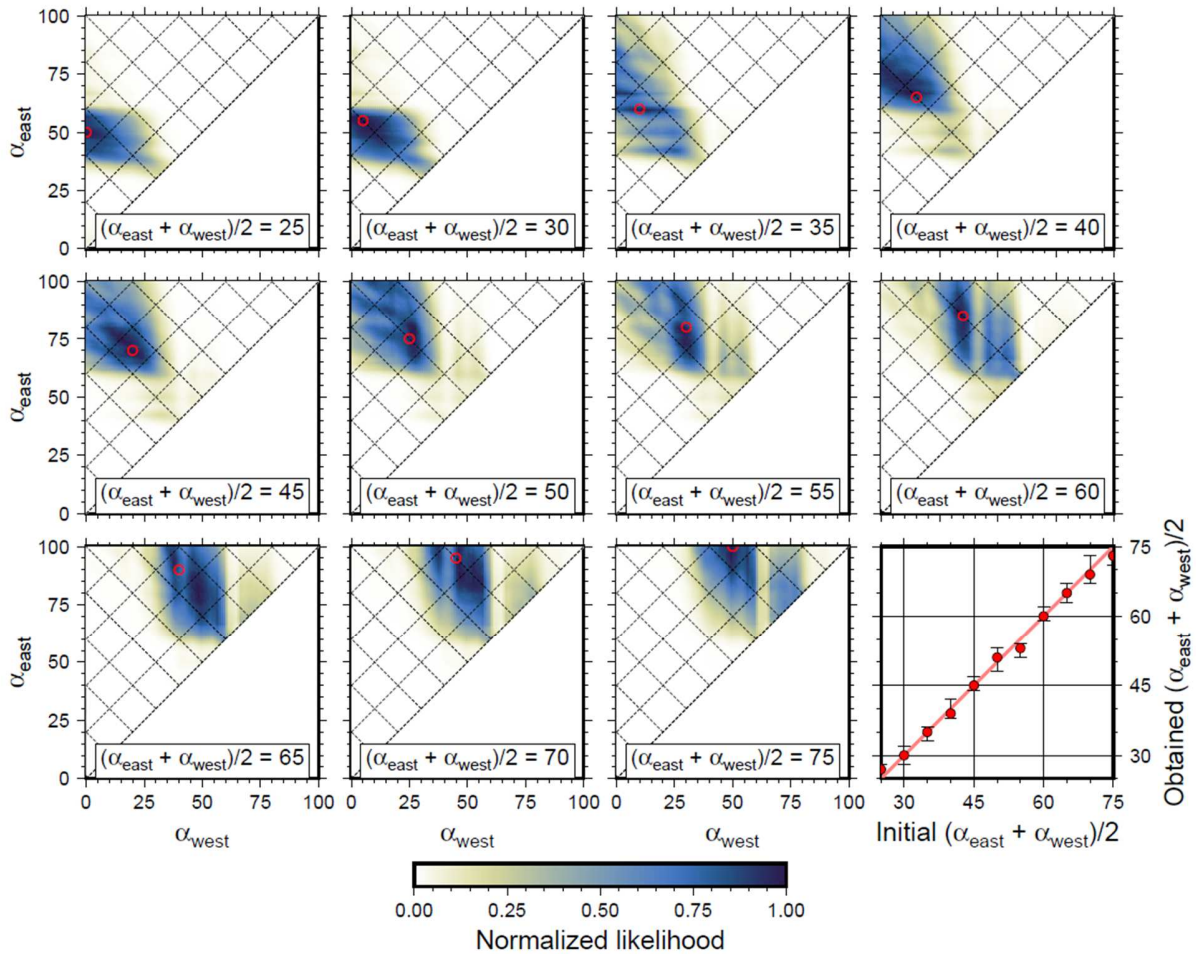
692
693
694
695



696

697 Figure 9

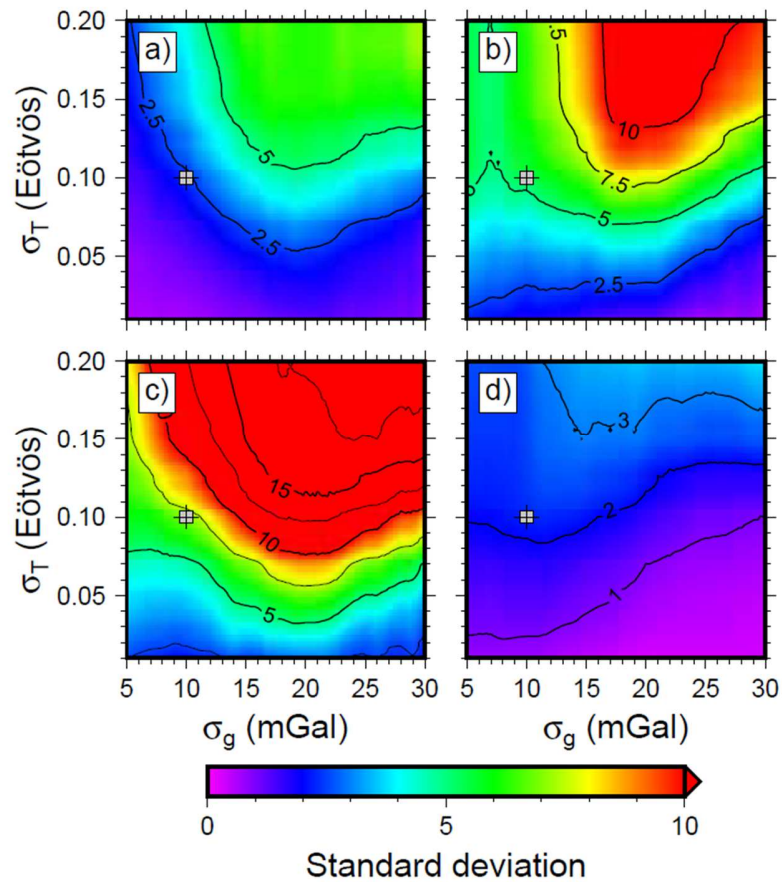
698 Synthetic tests assuming for the transition zone a constant mid-profile location ($[\alpha_{east} +$
699 $\alpha_{west}]/2 = 50$) and widths ranging between ca. 2.5 km ($\alpha_{east} - \alpha_{west} = 0.5$) and ca. 490 km
700 ($\alpha_{east} - \alpha_{west} = 100$). The color scale shows the calculated likelihood distribution obtained from
701 both gravity gradients and Bouguer anomaly (g_z and T_{ij}) assuming standard deviations of 0.1 E
702 and 10 mGal, respectively. The red circle shows the assumed initial coefficients α_{west} and α_{east}
703 of synthetic models. The bottom right figure gives a comparison between the initial and the
704 predicted $\alpha_{east} - \alpha_{west}$ values. The pink line corresponds to the first bisector ($y = x$).



705

706 Figure 10

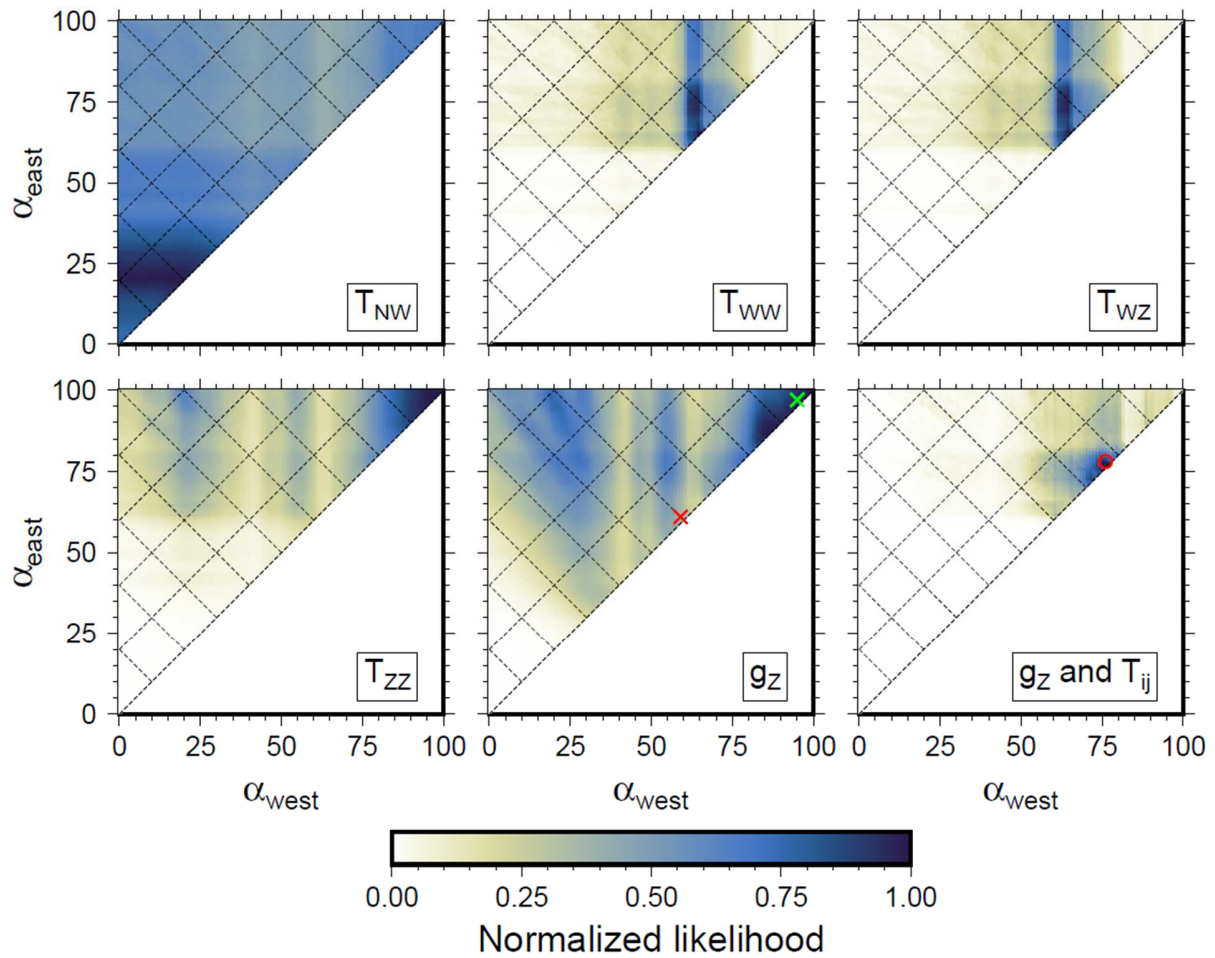
707 Synthetic tests assuming for the transition zone a constant width of ca. 250 km ($\alpha_{east} - \alpha_{west} =$
 708 50) and mid-profile located at different positions between central-eastern Nepal ($[\alpha_{east} +$
 709 $\alpha_{west}]/2 = 25$) and westernmost Bhutan ($[\alpha_{east} + \alpha_{west}]/2 = 75$). The color scale shows the
 710 calculated likelihood distribution obtained from both gravity gradients and Bouguer anomaly (g_z
 711 and T_{ij}) with standard deviations of $0.1 E$ and $10 mGal$, respectively. The red circle shows the
 712 assumed initial coefficients α_{west} and α_{east} of synthetic models. The bottom right figure gives a
 713 comparison between the initial and the predicted location of the transition zone. The pink line
 714 corresponds to the first bisector ($y = x$).



715

716 Figure 11

717 Synthetic test showing the effect of data dispersion in the variation of predicted coefficients. σ_g
 718 and σ_T are the assumed standard deviation of gravity and gravity gradient dataset, respectively.
 719 Gray squares indicate the standard deviations of 0.1 E and 10 mGal used in the reference
 720 model. Color scale gives the distribution of standard deviation in kilometers of the transition
 721 zone parameters: (a) the western boundary α_{west} , (b) the eastern boundary α_{east} , (c) the width
 722 $\alpha_{east} - \alpha_{west}$, and (d) the mid-profile location $[\alpha_{east} + \alpha_{west}]/2$.



723

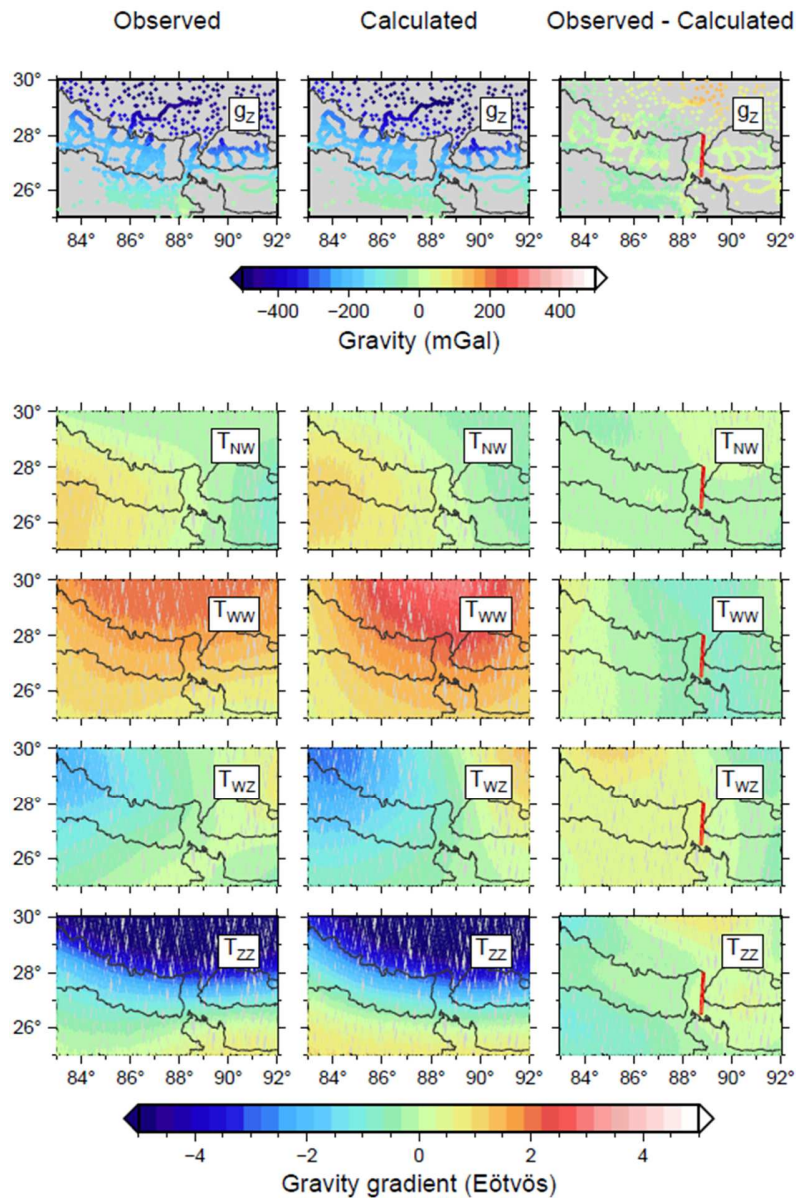
724 Figure 12

725 Normalized likelihood distribution obtained from gravity gradients and Bouguer anomaly
 726 observed between central Nepal and western Bhutan (see figures 5 and 6). $\sigma_T = 0.1 E$ and $\sigma_g =$
 727 $10 mGal$ are assumed for the standard deviations of gravity gradient and gravity dataset,
 728 respectively. The bottom center figure shows the result obtained from Bouguer anomaly. Red
 729 and green cross are associated with the models proposed by Hetényi et al. (2016) and Godin
 730 and Harris (2014), respectively. The bottom right figure gives the result obtained from both
 731 gravity and gravity gradients showing a likelihood maxima with $\alpha_{west} = 76$ and $\alpha_{east} = 78$ (red
 732 circle).

733

734

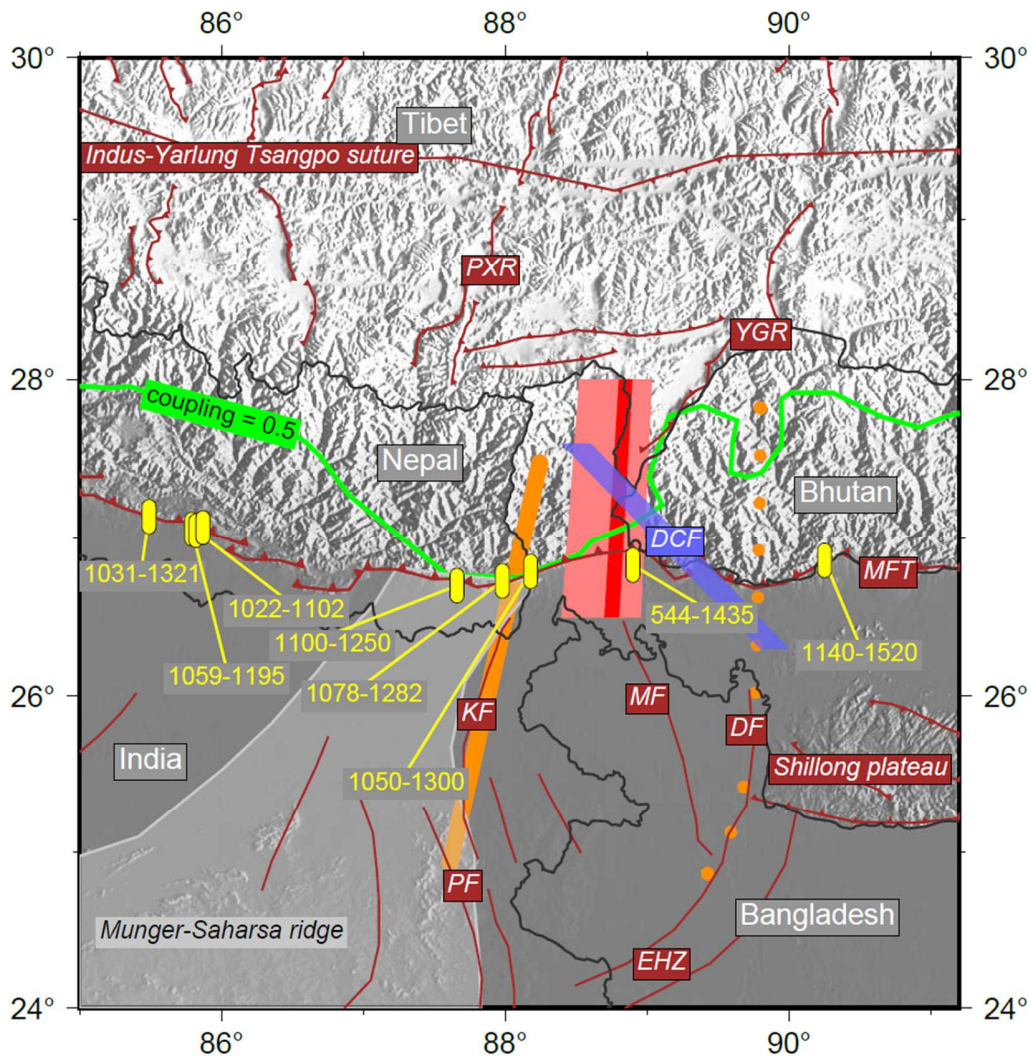
735
736



737

738 Figure 13

739 Comparison between observed and predicted gravity and gravity gradient from central Nepal to
740 western Bhutan. The first column summarizes the observations presented in figures 1 and 3.
741 The second column shows the gravity and gravity gradient calculated from our best-fitting
742 model, in which $\alpha_{west} = 76$ and $\alpha_{east} = 78$ (*width* ≈ 10 km and *mid-profile longitude* \approx
743 88.4°). The third column shows the difference between the observed and calculated gravity and
744 gravity gradient. The red narrow rectangle gives the location of the obtained transition zone. The
745 same color scale is used to plot observations, predicted fields, and their differences.
746



747

748 Figure 14

749 Map showing the location of the obtained transition zone between the Himalayan segments of
 750 Nepal and Bhutan. The red rectangle is associated with the best-fitting model, the pink rectangle
 751 represents a variance of 1 sigma. The orange lines are previously proposed segment
 752 boundaries by Hetényi et al. 2016 (solid) and Godin and Harris 2014 (dotted). Borders of India,
 753 Bangladesh, Nepal, Bhutan, and Tibet as well as major tectonic structures (DCF, Dhubri-
 754 Chungthang fault zone highlighted in blue; EHZ, Eocene Hinge Zone, KF, Kishanganj fault; MF,
 755 Madhupur fault; MFT, Main Frontal Thrust; PF, Pingla fault; PXR, Pumqu-Xainza rift; YGR,
 756 Yadong-Gulu rift; Indus-Yarlung suture) are shown as reference. Yellow rectangles give the
 757 location of study sites along the Main Frontal Thrust (MFT) modified from Wesnousky et al.
 758 (2019). Sites are labeled with the age range of paleoearthquakes. The green line depicts the
 759 contour line of interseismic coupling = 0.5 obtained by Dal Zilio et al. (2020). The light gray
 760 shaded patch indicates the extent of the Munger-Saharsa ridge.